Fully 3D numerical investigation of liquid jetting

Lopez Lopez, Jose L.

Award date:
2017

Technische Universiteit
Eindhoven
University of Technology

Department of Applied Physics
Turbulence and Vortex Dynamics (WDY)

Fully 3D numerical investigation of liquid jetting

Master Thesis

Jose Luis López López

Supervisors:
Prof.dr.F. Toschi
Prof.dr.ir.H.M.A. Wijshoff
ir. H. Reinten
Committe Members:
Prof.dr.H.J.H. Clercx
Dr.ir.L.P.G. Kamp

R-1923-A

16, August 2017,
Eindhoven, the Netherlands.

The study program and this thesis were funded by CONACyT-SENER, México.

Contents

Chapter 1

Introduction

Droplets formation from a liquid jet are ubiquitous in nature, water droplets dripping from a tap is a common example that we encounter in our everyday life. In fluid dynamics, a jet is a stream of fluid that is projected into a surrounding medium, usually from some kind of nozzle, aperture or orifice. An industrial application of liquid jetting is inkjet printing, where droplets are created in order to print patterns on paper. Recent advances in inkjet printing technology pose large demands to develop fundamental understanding of the forces and flow conditions that control the dynamics of the jettings.

This thesis investigates some aspects related to the fluid dynamics and numerical modeling of liquid jettings, motivated by inkjet printing applications. This problem involves multiphase flows in 3D complex geometries.

1.1 Drop on Demand (DoD) Inkjet printing

Inkjet printing technology is used to dispense picoliter volumes of liquids onto a substrate. A broad range of liquids can be dispensed, for example, inks, metals and even recently biological tissue [5]. Unlike traditional printing methods, which create a pattern by transferring liquids through a master stencil onto a substrate, inkjet printing progressively builds up patterns by depositing a large number of individual micrometer-size drops onto the substrate [9].

There exist different methods of inkjet printing, of which Continuous Inkjet (CIJ) and Drop on Demand (DoD) are two of the most important [5]. In CIJ, liquid is contained in a pressurized chamber and continuously flows through a nozzle, on which a periodic disturbance is applied to breakup the liquid jet into a continuous stream of drops. A complex process is used to select which drops reach the substrate in order to form the pattern. Unused drops are collected back into the printer. In contrast to CIJ printers, DoD inkjet printers do not use a continuum stream of drops. Instead, DoD inkjet printheads contain thousands of microscopic-size nozzles which can be individually controlled [20]. This method allows for a dynamic and more accurate control of drop deposition— doubted drop on demand (DoD). In this thesis, liquid jetting specifically in Piezo DoD inkjet nozzles is numerically investigated.

In a Piezo DoD inkjet nozzle unit, liquid jetting is controlled by applying a voltage signal to a piezoelectric material, which generates a pressure pulse that jets the liquid out of the nozzle. The amplitude, frequency and shape of this pressure pulse define the size, velocity and frequency of the droplets [4]. For optimal control of the drop formation process, it is extremely important to design a pressure pulse which considers both the characteristic features of the nozzle unit and the physical parameters of the liquid. Fig. 1.1 illustrates a typical piezo DoD inkjet nozzle unit. The main process in a piezo DoD inkjet nozzle unit can be summarized as follows: i) a voltage signal is applied to the piezo element, ii) the deformation of the piezo element generates a pressure pulse inside the liquid chamber, iii) this pressure pulse drives the liquid jetting, iv) resulting in the formation of a main drop and satellite droplets.

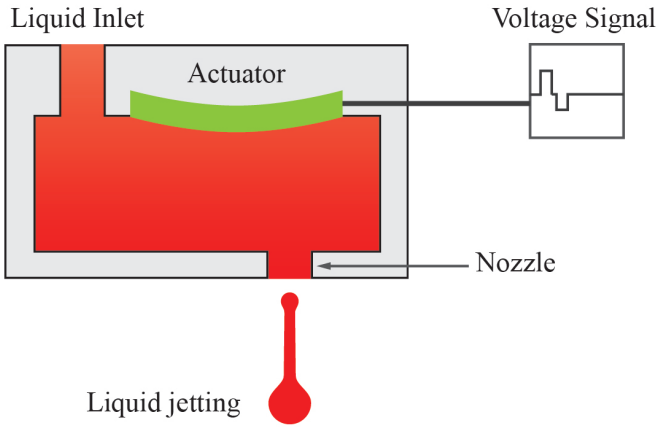

Figure 1.1: Schematic diagram of (DoD piezo) inkjet nozzle unit. In the nozzle unit, a voltage signal is applied to the piezo actuator, then the displacement of the piezo generates a pressure pulse that drives the liquid jetting.

1.2 Drop formation on DoD inkjet printing

Images of experimental DoD liquid jetting are presented in Fig. 1.2. The drop formation process in DoD liquid jetting can be described in three main stages. In the first stage, the ejection and stretching of the liquid is governed by inertia. In the second stage, the filament forms a head droplet and the liquid pinches-off from the nozzle exit due to surface tension. In the last stage, a tail droplet is formed and the filament may break up into satellite droplets due to Rayleigh Plateau instability [4]. Ideally, the jet should become a single spherical droplet before reaching the substrate, however the main droplet is commonly followed by a set of small satellite droplets. The diameter of the main droplet is determined by the size of the nozzle, both of which typically vary from 10 to 100 [μm]. The volumes of these droplets are of the order of 0.5 to 500 [pl] [4]. The velocity of the main droplet typically ranges between 5 to 8 [ms^{-1}] [9]. In Fig. 1.2 the image on the left shows a droplet that was ejected with a lower amplitude actuation signal than the droplet on the right image. This amplitude of the actuation signal is directly proportional to the velocity of the drop i.e the droplet on the left is slower than the droplet on the right. The faster jet breaks up into satellite droplets.

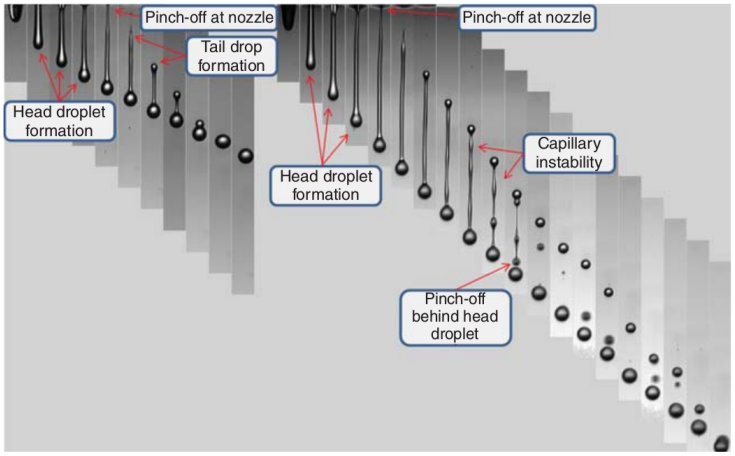

Figure 1.2: Experimental images of liquid jetting in a piezo DoD inkjet printer. The left and right images represent two different voltage actuation signals. The left side liquid jetting was generated with a lower amplitude signal than the amplitude the one on the right hand side image. The amplitude of the actuation signal is directly proportional to the velocity of the drop, which in fact shows that higher velocities result in a higher number of satellite droplets, figure reproduced from [4].

1.3 Numerical modeling of liquid jetting

Performing experimental studies on liquid jetting in inkjet printers is a complex task because of the size and speed of the droplets. It requires either ultra high-speed imaging techniques at frame rates of 1 million frames per second or stroboscopic techniques with illumination times $< 20 \quad [ns]$ ([5]). Experimental studies on drop formation and nozzle-fluid interaction have three main limitations. The first restriction is on the liquid, as one can not investigate all sort of liquids i.e. the whole parameter space of the liquid. Secondly, the nozzles material, shape, and wetting condition can not be chosen arbitrarily. Lastly, the processes inside the nozzle chamber, such as bubble entrainment [10], are difficult to be measured.

In contrast, numerical modeling of liquid jetting offers, in principle, the possibility to explore the parameter space of the liquid and can reveal detailed information about the fluid dynamics throughout the entire liquid jetting process [5]. Numerical modeling also provides information about interactions between the liquid and the nozzle, such as the dynamics of the contact line [16]. For these reasons, numerical modeling is often used to complement experimental studies and is widely used in the design of droplet production systems [3]. Although numerical modeling has many advantages over experimental studies, modeling liquid jetting presents its own challenges. When simulating free surface flows, special mathematical treatments are required to model the singularities that appear in the pinch-off of liquid jets [3]. Modeling surface tension driven flows also requires complex and computationally expensive algorithms to track the fluid-fluid interface [13].

In this context, the Lattice Boltzmann Method (LBM) has shown promising results for simulating free surface multiphase flows in complex geometries [8]. Multiphase LBM has already been applied to simulate Piezo DoD liquid jetting in 2D [7] and 2D axisymmetric systems [16], however fully 3D numerical simulations could give a deeper insight about the physics behind liquid jetting. Particularly, 3D simulations are necessary when the features to be measured are not axisymmetric, for example, the effects caused by structural defects in the nozzle.

The research collaboration between the Vortex and turbulence dynamics group (WDY) at Eindhoven University of Technology and the R&D department at Océ technologies aims to develop a numerical toolbox to accurately and efficiently study fully 3D liquid jetting. This thesis focuses in developing and using this toolbox to study the role of nozzle wettability in inkjet printing.

1.4 Outline of the thesis

Chapter 2 provides the theoretical background for the numerical study of liquid jetting. Here we briefly describe the concepts, definitions, and laws which are necessary for the understanding of the problem and that are used in the rest of the thesis.

Chapter 3 provides an overview of the Lattice Boltzmann method for multiphase flows. In this chapter, we discuss the boundary conditions and force implementation in the method. Here we provide a detailed analysis of the Kupershtokh multiphase model, which helps us to understand some of the strengths and limitations of the model. We conclude this chapter with a discussion of the implementation of the wetting conditions in the Kupershtokh method.

Chapter 4 presents the numerical simulations of liquid jetting in inkjet printing. This chapter describes the important aspects of the LB model to study liquid jetting: first a non-dimensional analysis shows that we are capable of simulating real inkjet printing systems in 3D; second we discuss the constraints that must be taken in account while choosing the LB parameters; third we introduced a way to convert the LB simulations to SI units and vice versa; and finally we present fully 3D simulations of a real inkjet printing system and we present results of the role of non-homogeneous nozzle wettabilitty in the liquid jetting.

Finally, in chapter 5, we draw conclusions from our research and give recommendations that may be used in the future for continuation and extension of the research presented in this thesis.

Chapter 2

Theoretical background

This chapter provides the essential theoretical background information used in the rest of the thesis. This includes, the mass and momentum conservation equations, the equations of state, the basic concepts behind the Lattice Boltzmann equation, as well as essential features of the interfacial phenomena between fluids and solids.

2.1 Hydrodynamics and Kinetic Theory

The continuity, momentum (Navier-Stokes) and energy equations are reviewed in the first part of this section. In the second part, the basic of kinetic molecular theory are presented.

2.1.1 Navier Stokes and Continuum Theory

Continuity equation

In fluid dynamics we assume that fluids are described by continuous hydrodynamic fields, such as density and velocity. Let us consider a small fluid element with density ρ which occupies some volume V_0. By conservation of mass, the change of the mass in this fluid element per unit time, must equal the amount of fluid flowing into or out of this fluid element. Mathematically this is expressed by

$$\frac{\partial}{\partial t}\int_{V_0}\rho dV = -\oint_{\partial V_0}\rho\mathbf{u}\cdot d\mathbf{A} \tag{2.1}$$

where conventionally one takes $d\mathbf{A}$ as the outward normal direction to the surface. The surface integral on the RHS can be transformed into a volume integral by using the divergence theorem and by removing the volume contribution, we obtain:

$$\frac{\partial\rho}{\partial t} + \nabla\cdot(\rho\mathbf{u}) = 0 \tag{2.2}$$

where $\mathbf{u}$ is the fluid velocity and $\rho\mathbf{u} = \mathbf{j}$ is the momentum density or mass flux density.

If the fluid element is not at a fixed point in space, the continuity equation can be written in the form

$$\frac{D\rho}{Dt} + \rho\nabla\cdot\mathbf{u} = 0 \tag{2.3}$$

here we introduced the material derivative, defined as

$$\frac{D}{Dt} = \frac{\partial}{\partial t} + \mathbf{u}\cdot\nabla \tag{2.4}$$

which denotes the rate of change of the fluid element moving in space.

For a general conserved quantity, ϕ, fluid conservation equations can be given in two main forms: conservation form, or material derivative form. The two forms can be related as

$$\frac{\partial(\phi)}{\partial t} + \nabla \cdot (\mathbf{u}\phi) = \frac{D\phi}{Dt} \tag{2.5}$$

Navier-Stokes Equation

Consider the change of momentum for a fluid element with density ρ and velocity $\mathbf{u}$ occupying a volume V_0. Ideally, the change of net momentum can be due to (i) flow of momentum into or out the fluid element, (ii) differences in pressure p and (iii) external body forces $\mathbf{F}$. Those contributions are mathematically expressed in the momentum balance equation:

$$\frac{d}{dt}\int_{V_0} \rho\mathbf{u}dV = -\oint_{\partial V_0} \rho\mathbf{u}\mathbf{u}\cdot d\mathbf{A} - \oint_{\partial V_0} pd\mathbf{A} + \int_{V_0} \mathbf{F}dV \tag{2.6}$$

where $\mathbf{uu}$ denotes the outer (tensor) product with components $u_\alpha u_\beta$. By transforming the surface integrals into volume integrals, using the divergence theorem and removing the volume contribution, the above equation leads to the Euler equation:

$$\frac{\partial(\rho\mathbf{u})}{\partial t} + \nabla \cdot (\rho\mathbf{u}\mathbf{u}) = -\nabla p + \mathbf{F} \tag{2.7}$$

a PDE describing the conservation of momentum for an ideal (i.e non viscous) fluid. The general form of the momentum equation is called the Cauchy momentum equation:

$$\frac{\partial(\rho\mathbf{u})}{\partial t} + \nabla \cdot \mathbf{\Pi} = \boldsymbol{F} \tag{2.8}$$

where $\mathbf{\Pi}$ is the momentum flux density tensor:

$$\Pi_{\alpha\beta} = \rho u_\alpha u_\beta - \sigma_{\alpha\beta} \tag{2.9}$$

The term $\sigma_{\alpha\beta}$ is called the stress tensor and it corresponds to the non-direct momentum transfer of the moving fluid. For simple fluids described by the Euler equation we find an isotropic stress $\sigma_{\alpha\beta} = -p\delta_{\alpha\beta}$ i.e. the diagonal elements.

In the Euler equation the momentum flux does not include the contribution of viscosity, which causes dissipative and irreversible transfer of momentum from one fluid element to another. The general form of the stress tensor includes the contribution of viscosity. Assume that this contribution is zero for a uniform flow and that for small velocity gradients the momentum transfer due to viscosity is represented by terms which are proportional to the first derivative of the velocity [11]. Under those assumptions the second rank stress tensor is

$$\sigma'_{\alpha\beta} = \eta\left(\frac{\partial u_\alpha}{\partial x_\beta} + \frac{\partial u_\beta}{\partial x_\alpha}\right) + \xi\delta_{\alpha\beta}\frac{\delta u_\gamma}{\partial x_\gamma} \tag{2.10}$$

where η and ξ are coefficients of viscosity. The viscous stress tensor is often separated in two terms: shear stress and a normal stress [11]:

$$\sigma'_{\alpha\beta} = \eta\left(\frac{\partial u_\alpha}{\partial x_\beta} + \frac{\partial u_\beta}{\partial x_\alpha} - \frac{2}{3}\delta_{\alpha\beta}\frac{\partial u_\gamma}{\partial x_\gamma}\right) + \eta_B\delta_{\alpha\beta}\frac{\partial u_\gamma}{\partial x_\gamma} \tag{2.11}$$

Here η is called the shear viscosity and $\eta_B = 2\eta/3 + \xi$ is called the bulk viscosity.

Consider the total stress tensor as follows

$$\sigma_{\alpha\beta} = \sigma'_{\alpha\beta} - p\delta_{\alpha\beta} \tag{2.12}$$

where p is the pressure. In this context, the Navier-Stokes equation is

$$\frac{\partial(\rho u_\alpha)}{\partial t} + \frac{\partial(\rho u_\alpha u_\beta)}{\partial x_\beta} = -\frac{\partial p}{\partial x_\beta}\left[\eta\left(\frac{\partial u_\alpha}{\partial x_\beta} + \frac{\partial u_\beta}{\partial x_\alpha}\right) + \left(\eta_B - \frac{2\eta}{3}\right)\frac{u_\gamma}{\partial x_\gamma}\delta_{\alpha\beta}\right] + F_\alpha \tag{2.13}$$

for a constant viscosities, follows

$$\rho\frac{Du_\alpha}{\partial x_\alpha}+\eta\frac{\partial^2 u_\alpha}{\partial x_\beta x_\beta}+\left(\eta_B+\frac{\eta}{3}\right)\frac{\partial^2 u_\alpha}{\partial x_\alpha x_\beta}+F_\alpha \tag{2.14}$$

Assuming $\rho = constant$, which implies $\nabla \cdot \boldsymbol{u} = 0$, the incompressible Navier-Stokes equation becomes

$$\rho\frac{D\boldsymbol{u}}{Dt} = -\nabla p + \eta\Delta\boldsymbol{u} + \boldsymbol{F} \tag{2.15}$$

where Δ is the Laplace operator.

Equations of state

To describe the fluid system we use the continuity equation, which describes the conservation of mass, and the Navier-Stokes equation (one for each spatial component), which describes the conservation of momentum. The two equations constitute a system of four equations, however we have five unknowns, density ρ, pressure p, and the three velocity components u_x, u_y, u_z. To close the system we can include another equation by using the state principle of equilibrium thermodynamics. This principle relates the thermodynamic variables that describe the local thermodynamic state of the system. The principle states that any of the state variables such as density ρ, pressure p, temperature T, internal energy e, and the entropy s can be related to any other two state variables through an equation of state [11].

Consider the ideal gas law as a equation of state:

$$p = \rho RT \tag{2.16}$$

where R is the specific gas constant. The ideal gas law relates the pressure, temperature and density, which implies that we have now five equations but six variables including the temperature T. The system is still not mathematically solvable, some approximations are necessary. One of the possible approximations is the isothermal equation of state, which is central to the LBM. Consider the fluid as having a constant temperature $T \approx T_0$, in this case the isothermal EOS is

$$p = \rho RT_0 \tag{2.17}$$

here the pressure p is linearly related to the density ρ. The incompressible approximation is also commonly applied, it takes a density constant $\rho = \rho_0$. In this case the continuity equation $\nabla \cdot \boldsymbol{u}$ and N-S equations are themselves sufficient. Those equations form a closed system of four variables and four equations.

The van der Waals EOS can describe the behaviour of many real fluids [8]. It is given by

$$p = \frac{RT}{V_m - b} - a\left(\frac{1}{V_m}\right)^2 \tag{2.18}$$

where $V_m = V/n$ is the volume occupied by one mol of substance at a particular pressure and temperature, a is a parameter that characterize the attraction between molecules, and b is a minimum molar volume such that as V_m approaches b, no further compression is possible and the pressure rises rapidly.

2.1.2 Mesoscopic scale

In computational fluid dynamics, we often use the length and time scales of the fluid system to categorize the regime of our simulations. The three common descriptions are: microscopic, mesoscopic and macroscopic, as we can see in Fig. 2.1. Microscopic usually denotes a molecular level description. Macroscopic refers to a fully continuum picture, which is commonly used in traditional CFD methods. In between those scales, the mesoscopic description uses kinetic theory to track representative collections of molecules. LBM is a mesoscopic numerical method based on kinetic theory.

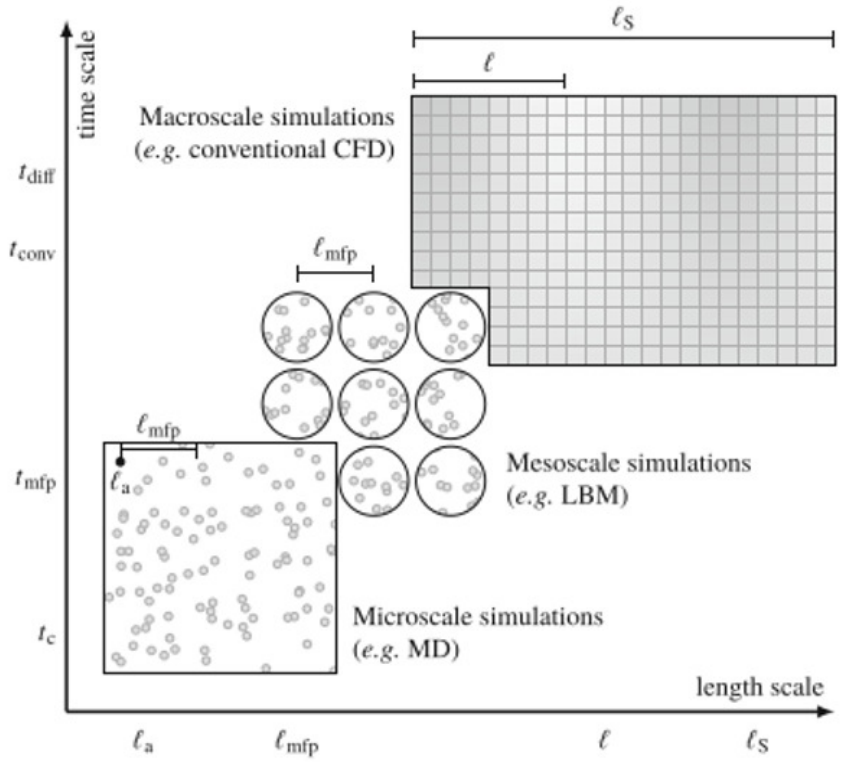

Figure 2.1: Hierarchy of length and time scales in computational fluid dynamics. Reproduced from [11].

Length scales

From small to large in a classical mechanics description [11], we have: the size of the fluid atom or molecule l_a, the mean free path of the particle l_{mfp}, the typical scale of gradients in some macroscopic properties l, and the system size l_s. The ordering of those length scales as illustrated in Fig. 2.1, is:

$$l_a \ll l_{mfp} \ll l \leq l_s \tag{2.19}$$

Time scales

For the description of fluids, we consider the collision time t_c scale as the shortest time scale. This collision time represents the duration of a collision event $l_c \sim \frac{l_a}{v_T}$, which is closely related to the thermal fluctuations of the system by the average thermal velocity of the molecules $v_T = (k_B T/m)^{1/2}$ [11]. It is common to assume that collisions happen instantaneously if $t_c \to 0$. The time scale for the kinetic theory description is $t_{mpf} = \frac{l_{mpf}}{v_t}$, and on this time scale the system relaxes to local equilibrium through collision events [11]. Local equilibrium does not imply global equilibrium.

Hydrodynamic effects appear at relatively large time and length scales. The shortest times at this scales are the convective $t_{conv} \sim \frac{l}{u}$ and the diffusive $t_{diff} \sim \frac{l^2}{\nu}$ time scales., where u is the macroscopic fluid velocity and ν is the kinematic viscosity. The Reynolds number can be defined as the ratio between those two time scales as follows

$$Re = \frac{t_{diff}}{t_{conv}} = \frac{ul}{\nu} \tag{2.20}$$

Another time scale which is very important in the LBM formulation is the acoustic time scale

$t_{sound} \sim \frac{l}{c_s}$, where c_s is the speed of sound in the fluid. If the sound time scale is faster than the advection time scale, the fluid behaves similarly to an incompressible fluid [11]. To characterize the compressibility of the fluid system, we can define the Mach number

$$Ma = \frac{t_{sound}}{t_{conv}} = \frac{u}{c_s} \tag{2.21}$$

for values of $Ma \leq 0.1$ we can assume incompressible flow. This assumption is very important in LBM, and gives a quote for the maximum velocities allowed in our simulations.

In extreme cases the hierarchy of length scales does not follow the one presented above. Consider a nanofluidic device, in those systems the mean free path l_{mfp} can be of comparable magnitude of one length scale of the system size $l_s \sim l_{mfp}$. To characterize those length scales we can employ the Knudsen number

$$K_n = \frac{l_{mfp}}{l} \tag{2.22}$$

for $K_n \ll 1$ the system is well described by Navier-Stokes equation, but for $K_n \sim 1$ we have to use the kinetic theory description [11]. The K_n is an important piece in the theoretical development of LBM, we will see later that it is used in the Chapman-Enskog expansion.

2.1.3 Kinetic theory

As we mentioned before, LBM lies on the mesoscopic length and time scale, as a result we need kinetic theory to describe the systems. For simplicity we will consider a dilute gas, i.e we will assume that $t_c \ll t_{mfp}$. In this description we will not consider polyatomic gases, i.e. we will not consider inelastic collisions.

The distribution function

We can consider the distribution function $f(\boldsymbol{x}, \boldsymbol{\xi}, t)$ as a representation of the density of mass in both three-dimensional physical space and in three dimensional velocity space [11]. Therefore, f has the units

$$[f] = \frac{kgs^3}{m^6} \tag{2.23}$$

in this sense, $f(\boldsymbol{x}, \boldsymbol{\xi}, t)$ can be seen as the density of particles with velocity $\boldsymbol{\xi}$ at position $\boldsymbol{x}$ and time t. By calculating the momenta of f, one can obtain the macroscopic variables such as mass density ρ, momentum density $\rho\boldsymbol{u}$, and total energy density ρE, as follows

$$\rho(\boldsymbol{x}, t) = \int f(\boldsymbol{x}, \boldsymbol{\xi}, t) d^3\xi \tag{2.24a}$$

$$\rho(\boldsymbol{x}, t)\boldsymbol{u}(\boldsymbol{x}, t) = \int \boldsymbol{\xi} f(\boldsymbol{x}, \boldsymbol{\xi}, t) d^3\xi \tag{2.24b}$$

$$\rho(\boldsymbol{x}, t)E(\boldsymbol{x}, t) = \frac{1}{2}\int |\boldsymbol{\xi}|^2 f(\boldsymbol{x}, \boldsymbol{\xi}, t) d^3\xi \tag{2.24c}$$

The equilibrium distribution function

Due to the collisions between molecules, if the gas is left alone for a sufficient long time, one can assume that $f(\boldsymbol{x}, \boldsymbol{\xi}, t)$ will reach an equilibrium distribution, $f^{eq}(\boldsymbol{x}, \boldsymbol{\xi}, t)$, which is isotropic in velocity space around $\boldsymbol{\xi} = \boldsymbol{u}$ [11], where $\boldsymbol{u}$ is the mean velocity. If we see our system from a reference frame moving with speed $\boldsymbol{u}$, the equilibrium distribution can be expressed as $f^{eq}(\boldsymbol{x}, |\boldsymbol{v}|, t)$. By considering f^{eq} as a separable solution, and by using the ideal gas and statistical mechanics, the equilibrium distribution can be found to be [11]

$$f^{eq}(\boldsymbol{x}, |\boldsymbol{v}|, t) = \rho\left(\frac{3}{4\pi e}\right)^{3/2} e^{-3|\boldsymbol{v}|^2/(4e)} = \rho\left(\frac{1}{2\pi RT}\right)^{3/2} e^{-|\boldsymbol{v}|^2/(2RT)} \tag{2.25}$$

The Boltzmann Equation and the Collision Operator

We want to obtain the evolution of the distribution function $f = f(\boldsymbol{x}, \boldsymbol{\xi}, t)$. In order for obtaining that one can start by expressing the total derivative of f with respect to time t as:

$$\frac{df}{dt} = \left(\frac{\partial f}{\partial t}\right)\frac{dt}{dt} + \left(\frac{\partial f}{\partial x_\beta}\right)\frac{dx_\beta}{dt} + \left(\frac{\partial f}{\partial \xi_\beta}\right)\frac{d\xi_\beta}{dt} \tag{2.26}$$

here $\frac{d\boldsymbol{x}_\beta}{dt} = \xi_\beta$ and from Newton's second law $\frac{d\xi_\beta}{dt} = \frac{F_\beta}{\rho}$ [11].
By applying the reasoning developed above, the Boltzmann equation is

$$\frac{\partial f}{\partial t} + \xi_\beta \frac{\partial f}{\partial x_\beta} + \frac{F_\beta}{\rho}\frac{\partial f}{\partial \xi_\beta} = \Omega(f) \tag{2.27}$$

this equation can be seen as an advection type equation, where the first two terms represent the distribution function being advected with the velocity $\boldsymbol{\xi}$ of its particles and $\Omega(f)$ is called the collision operator.

The conservation of mass, momentum and energy can be expressed in terms of the moments of the collision operator $\Omega(f)$, as follows:

$$mass: \qquad \int \Omega(f) d^3\xi = 0 \tag{2.28a}$$

$$momentum: \qquad \int \boldsymbol{\xi}\Omega(f) d^3\xi = \mathbf{0} \tag{2.28b}$$

$$energy: \qquad \int |\boldsymbol{\xi}|^2 \Omega(f) d^3\xi = 0 \tag{2.28c}$$

In LBM one often uses a simplified version of the collision operator. One of the possible simplifications is the well known Bhatnagar, Gross and Krook (BGK) collision operator

$$\Omega(f) = -\frac{1}{\tau}(f - f^{eq}) \tag{2.29}$$

it accounts for the relaxation of the distribution function towards the equilibrium distribution. The constant τ determines the speed of this equilibration, and it is a very important parameter in the LBM simulations, as we will see later, eg. the value of τ is directly related with the viscosity of the system.

Macroscopic conservation equations

The moments of the Boltzmann equation over the velocity space provide the macroscopic equations of fluid mechanics. The moments are [11]

$$\Pi_0 = \int f d^3\xi = \rho \qquad \Pi_\alpha = \int \xi_\alpha f d^3\xi = \rho u_\alpha \tag{2.30a}$$

$$\Pi_{\alpha\beta} = \int \xi_\alpha \xi_\beta f d^3\xi \qquad \Pi_{\alpha\beta\gamma} = \int \xi_\alpha \xi_\beta \xi_\gamma f d^3\xi \tag{2.30b}$$

here the second order momenta $\Pi_{\alpha\beta}$ is found to be the momentum flux tensor, which was introduced before in the Cauchy equation (2.8). To obtain the conservation equations we need the next result, which can be found by using multidimensional integration by parts [11]

$$\int \frac{\partial f}{\partial \xi_\beta} d^3\xi = 0 \tag{2.31a}$$

$$\int \xi_\alpha \frac{\partial f}{\partial \xi_\beta} d^3\xi = -\int \frac{\partial \xi_\alpha}{\partial \xi_\beta} f d^3\xi = -\rho\delta_{\alpha\beta} \tag{2.31b}$$

$$\int \xi_\alpha \xi_\alpha \frac{\partial f}{\partial \xi_\beta} d^3\xi = -\int \frac{\partial(\xi_\alpha \xi_\alpha)}{\partial \xi_\beta} f d^3\xi = -2\rho u_\beta \tag{2.31c}$$

at this point one can obtain the mass, momentum and energy conservation equations, respectively, as follows:

$$\frac{\partial \rho}{\partial t} + \frac{\partial(\rho u_\beta)}{\partial x_\beta} = 0, \tag{2.32a}$$

$$\frac{\partial(\rho u_\alpha)}{\partial t} + \frac{\partial \Pi_{\alpha\beta}}{\partial x_\beta} = F_\alpha, \tag{2.32b}$$

$$\frac{\partial(\rho E)}{\partial t} + \frac{1}{2}\frac{\partial \Pi_{\alpha\alpha\beta}}{\partial x_\beta} = F_\beta u_\beta. \tag{2.32c}$$

2.2 Surface tension

An insect walking on water is shown in Fig. 2.2. Those insects can walk on water as a consequence of surface tension, a thermodynamic material property for a system maintaining liquid-liquid or liquid-air interfaces. On the region between the liquid and gas, the density changes smoothly.

Figure 2.2: Water strider walking on the liquid-air interphase, figure reproduced from [6].

This transition layer is of the order of nanometers for common thermodynamic conditions. As a result, the transition layer is very small compared with the size of a macroscopic system. From a mechanical description, the effect of surface tension have two manifestations; i) a force per unit length acting on the molecules which lie close to the interfacial region. ii) A pressure jump across a curved interface, which is known as the capillary pressure. These pressure difference can be described by the Young-Laplace law [1]:

$$\Delta p = \gamma \left(\frac{1}{R_1} + \frac{1}{R_2} \right) \tag{2.33}$$

here $R_{1,2}$ are the radii of curvature of a general surface. In drops and bubbles, there is a pressure difference between the inside and outside. The pressure is always higher on the inside of the bubble, or drop, and it reduces to

$$\Delta p = \frac{2\gamma}{R} \tag{2.34}$$

In this thesis, we will use this mathematical expression to estimate the surface tension on the interface between the liquid and vapor in our Lattice Boltzmann simulations.

2.2.1 Contact angle

The contact angle of a liquid on a solid is a parameter that quantifies the affinity of the liquid to this material. The contact angle is defined as the angle formed by the intersection of the liquid-solid interface and the liquid-vapor interface, as shown in Fig. 2.3. The Young equation describes

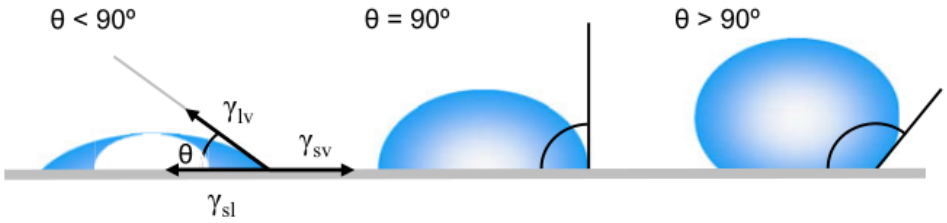

Figure 2.3: Image of contact angles formed by droplets resting on a flat solid surface, figure reproduced from [22]. Here θ is the contact angle, γ_{lv}, γ_{sv} and γ_{sl} are the liquid-vapor, solid-vapor, and solid-liquid interfacial tensions.

the mechanical equilibrium of the droplet on a solid surface

$$\gamma_{lv} cos\theta = \gamma_{sv} - \gamma_{sl} \tag{2.35}$$

here θ is the contact angle; γ_{lv}, γsv, and γ_{sl} are the liquid-vapor, solid-vapor, and solid-liquid interfacial tensions. It is common to consider consider that a droplet wets the solid for values of $\theta < 90$ and that the droplet non-wets the solid for values of $\theta > 90$. In this thesis, we will study the role of the wettability conditions on the nozzle of the inkjet printer.

In this chapter we provided the essential background information that will be used in this thesis. In the next chapter, we continue with a detailed overview of the Lattice Boltzmann method for multiphase flows. This computational method will be used to simulate the liquid jetting.

Chapter 3

Simulation method

In the previous chapters we have motivated the problem of liquid jetting in inkjet printing and described the fluid dynamics theory behind this process. Next, we numerically model the problem by using the Lattice Boltzmann Method for fluid dynamics. In this chapter, we introduce the Lattice Boltzmann Method (LBM), including the typical lattices and the basic algorithms used to impose boundary conditions. Since our problem involves a liquid surrounded by a vapor, a multiphase LBM model known as the multiphase Kupershtokh model is introduced here. Finally, we describe a procedure for estimating surface tension and discuss the implementation of the wetting conditions for our model.

3.1 The Lattice Boltzmann Method

The Lattice Boltzmann method is a discretization of the continuous Boltzmann equation (Eq. 2.27). In our model, the collision operator is simplified by using the single relaxation time BGK approximation (Eq. 2.29). In absence of external forces, the discretized Boltzmann equation for a finite set of m velocity vectors $\boldsymbol{c}_i$ can be expressed as:

$$\frac{\partial f_i}{\partial t} + \boldsymbol{c}_i \cdot \nabla f_i = -\frac{1}{\tau}(f_i - f_i^{eq}), \qquad (i = 0, 1 \cdots, m-1), \tag{3.1}$$

where $f_i \equiv f(\boldsymbol{v}, \boldsymbol{c}, t)$, m is the number of discrete velocities and τ the single relaxation time from the BGK approximation. The function f_i^{eq} is the equilibrium distribution function which in its discrete form is given by

$$f_i^{eq} = \rho[a + b(\boldsymbol{c}_i \cdot \boldsymbol{u} + c(\boldsymbol{c}_i \cdot \boldsymbol{u})^2 + d(\boldsymbol{u} \cdot \boldsymbol{u})^2] \tag{3.2}$$

where the constants a, b, c and d depend on the choice of the lattice. The macroscopic variables, mass density, ρ, and velocity, $\boldsymbol{u}$, are defined as:

$$\rho(\boldsymbol{x}, t) = \sum_{i=0}^{m-1} f_i(\boldsymbol{x}, t), \qquad \boldsymbol{u}(\boldsymbol{x}, t) = \frac{1}{\rho(\boldsymbol{x}, t)} \sum_{i=0}^{m-1} \boldsymbol{c}_i f_i(\boldsymbol{x}, t) \tag{3.3}$$

Fig. 3.1 shows the typical two (D2Q9) and three (D3Q19) dimensional lattices, with 9 and 19 velocities, respectively. The table 3.1 reports the properties of these lattices.

For the D2Q9 model, the equilibrium distribution function f^{eq} is defined in [19] as

$$f_i^{eq}(\boldsymbol{x}) = w_i \rho(\boldsymbol{x}) \left[1 + 3\frac{\boldsymbol{c}_i \cdot \boldsymbol{u}}{c_s^2} + \frac{9}{2}\frac{(\boldsymbol{c}_i \cdot \boldsymbol{u})^2}{c_s^4} - \frac{3}{2}\frac{\boldsymbol{u}^2}{c_s^2}\right] \tag{3.4}$$

where w_i are the weights, and $c_s = 1/\sqrt{3}$.

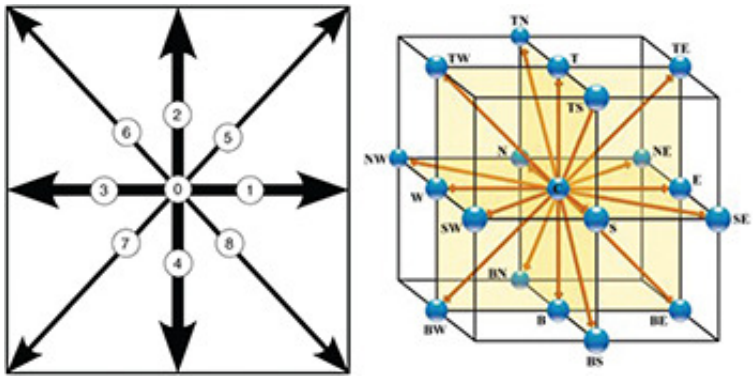

Figure 3.1: Illustration of typical two and three dimensional lattices. On the left the D2Q9 and on the right the D3Q19, with 9 and 19 discrete velocities, respectively, figure reproduced from [18].

Notation	Velocities $\boldsymbol{c}_i$	Number	Length $\lvert\boldsymbol{c}_i\rvert$	Weight w_i
D2Q9	$(0,0)$	1	0	4/9
	$(\pm1,0), \quad (0,\pm1)$	4	1	1/9
	$(\pm1,\pm1)$	4	$\sqrt{2}$	1/36
D3Q19	$(0,0,0)$	1	0	1/3
	$(\pm1,0,0), \quad (0,\pm1,0), \quad (0,0,\pm1)$	6	1	1/18
	$(\pm1,\pm1,0), \quad (\pm1,0,\pm1), \quad (0,\pm1,\pm1)$	12	$\sqrt{2}$	1/36

Table 3.1: Properties of the D2Q9 and D3Q19 lattices. The speed of sound for these velocity sets is $c_s = 1/\sqrt{3}$.

The time derivative in the BE (Eq. 3.1) is approximated by forward finite difference, and the spatial derivative by an upwind scheme [21], resulting in:

$$\frac{f_i(\boldsymbol{x},t+\Delta t)-f_i(\boldsymbol{x},t)}{\Delta t}+|\boldsymbol{c}_i|\frac{f_i(\boldsymbol{x},t)-f_i(\boldsymbol{x}-\boldsymbol{e}_i\Delta x_i,t)}{\Delta x_i}=-\frac{1}{\tau}[f_i(\boldsymbol{x}-\boldsymbol{e}_i\Delta x_i,t)-f^{eq}(\boldsymbol{x}-\boldsymbol{e}\Delta x_i,t)] \tag{3.5}$$

where $\boldsymbol{e}_i = \boldsymbol{c}_i/|\boldsymbol{c}_i|$ and $\Delta x_i = |\boldsymbol{x}-\boldsymbol{x}_i|$, and $\boldsymbol{x}$ is the nearest neighbor node in the $\boldsymbol{e}_i$ direction. From this equation, we can obtain the popular form of the Lattice Boltzmann equation [16] given by

$$f_i(\boldsymbol{x}+\boldsymbol{c}_i\Delta t,t+\Delta t)-f_i(\boldsymbol{x},t)=-\frac{\Delta t}{\tau}[f_i(\boldsymbol{x},t)-f_i^{eq}(\boldsymbol{x},t)] \tag{3.6}$$

where the equilibrium distribution function is given by (Eq. 3.2). Through a formal asymptotic technique called Chapman-Enskog method [17], the lattice Boltzmann Equation gives us the continuity equation and the N-S equations presented in section 2.1.1. This procedure shows that the dynamic viscosity μ and the thermodynamic pressure on the lattice are:

$$\mu=\nu\rho=\rho c_s^2\left(\tau-\frac{\Delta t}{2}\right), \qquad p=c_s^2\rho \tag{3.7}$$

where ν represent the kinematic viscosity, in addition, if $\tau \leq \Delta t/2$ the method becomes unstable. The term $c_s = \sqrt{dp/d\rho}$ can be interpreted as the speed of sound.

3.1.1 Forcing scheme in LBM

Body forces, such as gravity or intermolecular forces, can be included included in the numerical scheme. In this thesis, an intermolecular force between neighbor fluid nodes is introduced to

simulate the vapor-liquid phase transition. The LB equation which includes the body force is written as

$$f_i(\boldsymbol{x} + \boldsymbol{c}_i\Delta t, t + \Delta t) - f_i(\boldsymbol{x}, t) = -\frac{\Delta t}{\tau}[f_i(\boldsymbol{x}, t) - f_i^{eq}(\boldsymbol{x}, t)] + \Delta f_i \tag{3.8}$$

where Δf_i is the body force term. This term can be implemented in many different ways. In this thesis, we use the so called Exact Difference Method proposed by Kupershtokh [12]. In this scheme, the proposed force term is

$$\Delta f_i = f_i^{eq}(\rho, \boldsymbol{u} + \Delta\boldsymbol{u}) - f_i^{eq}(\rho, \boldsymbol{u}) \tag{3.9}$$

where $\Delta\boldsymbol{u} = \boldsymbol{F}\Delta t/\rho$. The real fluid velocity (Eq. 3.3) is then modified as follows

$$\boldsymbol{u} = \frac{1}{\rho}\left[\sum_i \boldsymbol{c}_i f_i + \frac{\boldsymbol{F}\Delta t}{2}\right] \tag{3.10}$$

here $\boldsymbol{u}$ is calculated at half time steps.

3.1.2 Units in The Lattice Boltzmann method

The elementary numerical units in LBM are presented in Tab. 3.2. All the physical quantities in the simulations can be expressed in terms of these elementary parameters.

	unit	symbol
Mass	mass unit	mu
Length	lattice unit	lu
Time	time step	ts
Temperature	temperature unit	tu

Table 3.2: Units in Lattice Boltzmann Methods.

3.2 Boundary conditions

Boundary conditions must be defined before we can obtain a solution for a given flow problem. In LBM we need boundary conditions for the distribution functions. It has been shown that non-slip and free-slip boundary conditions can be easily implemented [19]. In fact, this is one of the main advantages of LBM over traditional CFD methods. The basic forms of periodic, no-slip and open boundary conditions are described here.

3.2.1 Periodic boundary conditions

In periodic boundary conditions the system becomes closed by the edges, as if the flow leaving a boundary enters the opposite boundary. It implies that the flow properties at the east boundary are the same than the ones at the west boundary in Fig 3.2. The ghost nodes in the figure must be initialized before the streaming step. In our notation, periodic boundaries are implemented as:

$$f_i(\boldsymbol{X}'_{A,j}, t) = f_i(\boldsymbol{X}_{C,j}, t), \quad f_i(\boldsymbol{X}'_{C,j}, t) = f_i(\boldsymbol{X}_{A,j}, t) \tag{3.11}$$

where this relation holds for all times t, velocity directions i and indices j.

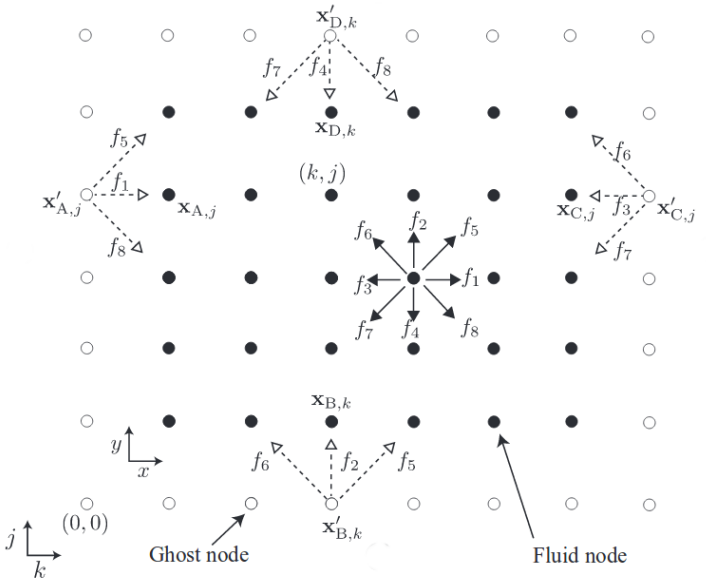

Figure 3.2: Illustration of the distribution functions at the boundary of D2Q9 lattice, reproduced from [16]. The solid dots are fluid nodes, and the hollow dots are ghost nodes, used to impose the periodic boundary conditions.

3.2.2 No-slip boundary condition

We use the bounceback algorithm [19] for the simulation of solid walls. The implementation of this is quite simple, one simply needs to designate a particular node as a solid obstacle and no special programming treatment is required. From Fig. 3.3, the standard bounceback boundary condition for D2Q9 model can be expressed as:

$$f_2(\boldsymbol{X}'_{B,k},t) = f_4(\boldsymbol{X}_{B,k},t), \qquad f_5(\boldsymbol{X}'_{B,k-1},t) = f_7(\boldsymbol{X}_{B,k},t), \qquad f_6(\boldsymbol{X}'_{B,k+1},t) = f_8(\boldsymbol{X}_{B,k},t) \tag{3.12}$$

where the same algorithm applies for all times.

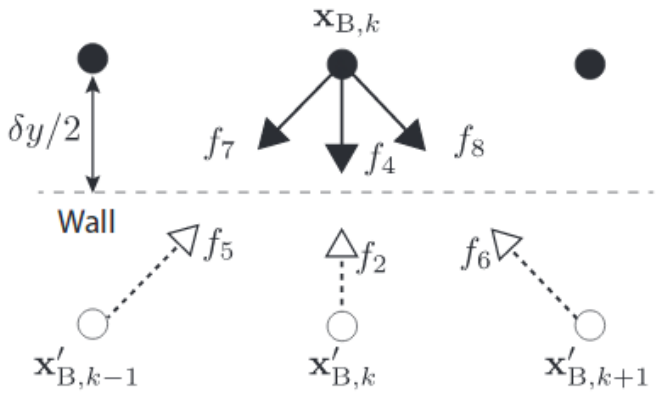

Figure 3.3: Illustration of the distribution functions for bounceback boundary conditions of D2Q9 lattice, reproduced from [16].

3.2.3 Open boundary condition

In this thesis, we use this condition on the upper-lower boundaries. For the LB simulations we apply this condition for the distribution functions [16].. We use the equilibrium distribution function given by Eq. (3.4) for the unknown values of $f_5(\boldsymbol{X}'_{B,k}, t), f_2(\boldsymbol{X}'_{B,k}, t), f_6(\boldsymbol{X}'_{B,k}, t)$ at the ghost nodes $\boldsymbol{X}'_B$, see Fig. 3.2. To calculate the equilibrium distribution function one requires the value of density and velocity at the ghost nodes. Different values of density and velocities lead to different values of the equilibrium distribution function. The choice of density and velocity at the ghost nodes impose different hydrodynamic boundary conditions.

3.3 Multiphase Lattice Boltzmann methods (LBM)

Multiphase LBM have become an efficient and robust technique for simulating complex flows that undergo phase transitions between liquid and vapor [8] [18]. The following are few of the advantages of multiphase LBM over traditional CFD methods:

1. In LBM non ideal equations of state can be incorporated to accurately describe both liquid and gas phases [12].
2. LBM automatically recovers the interfacial dynamics and explicit interface tracking is not required [8] [7] [12], which allows us to simulate coalescence and break up dynamics of the liquid jetting.
3. In LBM, complex solid boundaries with different wetting conditions are easily implemented, and the contact line dynamics on the nozzle can be accurately studied [16].
4. LBM has all the features of efficient parallel computing execution, which allows for fully 3D simulations at a reasonable computational time [17].

For these reasons, multiphase LBM are an excellent option for performing fully 3D simulations during the whole fluid dynamics process of liquid jetting. There exist many multiphase models for LBM, all of them with their own advantages and disadvantages [8]. In this research, the Kupershtokh [12] multiphase method is used. This model allows for incorporation of arbitrary EOS to describe the phase separation. In addition, the Kupershtokh model is able to achieve high density ratios $\sim 10^7$ between the liquid and vapor phases. These features of the Kupershtokh model are both key factors for simulations of liquid jetting in inkjet printing. In the next section, the Kupershtokh model will be described.

3.4 Kupershtokh multiphase LBM

Special mesoscopic forces are required for simulating the vapor-liquid phase transition in LBM. These forces act between every pair of neighbor nodes. One of the most typical LB multiphase models is the one implemented for Shan and Chen [19], where the total force acting on a fluid node is:

$$\boldsymbol{F}(\boldsymbol{x}) = \psi(\rho(\boldsymbol{x})) \sum_{i=1}^{N} w_i \psi(\rho(\boldsymbol{x} + \boldsymbol{e}_i))\boldsymbol{e}_i \tag{3.13}$$

where w_i are the coefficients for basic and diagonal directions in the lattice (see table 3.1), and ψ is the interaction potential:

$$\psi(\rho) = \rho_0(1 - \exp(-\rho/\rho_0)) \tag{3.14}$$

in this model, phase transition is possible for some values of ρ_0, which is an arbitrary constant. The EOS for this model has the form

$$P = \rho\theta - \alpha w_1 \psi^2 \tag{3.15}$$

where α and w_1 depend on the model, for example, $\alpha = 3/2$ and $w_1 = w_i/4$ in the D2Q9 model.

The Zhang and Chen multiphase model allows for incorporating arbitrary EOS [12]. In this model the total force acting on a fluid node is expressed as the gradient of a special potential, which depends on the EOS

$$\boldsymbol{F} = -\nabla U, \qquad U = P(\rho, T) - \rho\theta \tag{3.16}$$

The Kupershtokh model [12] is based on the Zhang and Chen model. In Kupershtokh, the mesoscopic force is expressed as a function of a special function Φ as follows

$$\boldsymbol{F} = \boldsymbol{F}(\nabla\Phi, \Phi) \tag{3.17}$$

where Φ is constructed in such a way that any arbitrary EOS can be included into the model and is defined as

$$\Phi(\bar{\rho}, \bar{T}) = \sqrt{-\bar{U}(\bar{\rho}, \bar{T})} \tag{3.18}$$

where $\bar{U}$ is the reduced potential $\bar{U} = U\Delta t^2/\rho_c h$, h is the lattice spacing.

In this case, $\bar{U} = k\bar{P} - \bar{\rho}\bar{\theta}$ represents a potential function which depends on the particular EOS, with $\bar{\theta} = \theta(\Delta t/h)^2 = 1/3$. The coefficient $k = \frac{P_c}{\rho_c}\frac{\Delta t^2}{h^2}$ is related to the simulated material, which for most inert gases it is $k \simeq 0.01$. Throughout this thesis, the van der Waals EOS will be used, and it can be expressed as

$$\bar{P} = \frac{8\bar{\rho}\bar{T}}{3 - \bar{\rho}} - 3\bar{\rho}^2 \tag{3.19}$$

where the quantities are expressed in reduced variables: $\bar{P} = P/P_c$, $\bar{\rho} = \rho/\rho_c$, $\bar{T} = T/T_c$, where T_c, P_c and ρ_c are the values at the critical point. The numerical approximation of this force for the D2Q9 and D3Q19 LBM models is

$$\boldsymbol{F} = \beta\left[A\sum_{i=1}^{N} w_i\Phi^2(\boldsymbol{x} + \boldsymbol{e}_i)\boldsymbol{e}_i + (1 - 2A)\Phi(\boldsymbol{x})\sum_{i=1}^{N} w_i\Phi(\boldsymbol{x} + \boldsymbol{e}_i)\boldsymbol{e}_i\right] \tag{3.20}$$

where $\boldsymbol{e}_i = \boldsymbol{c}_i\Delta t$ and the constant β is equal to 18/3 and 6 for the D2Q9 and D3Q19, respectively. In this force, the coefficient A is a free parameter which can be adjusted in order to fit the simulated and theoretical liquid-vapor coexistence curves.

Throughout this research the van der Waals EOS will be used. It was found in [12] that for the Kupershtokh model with vdW EOS, the simulated coexistence curve virtually coincides with the theoretical curve for temperatures $\bar{T}$ in the range $0.4 < \bar{T} < \bar{T}_c$. In addition, with this configuration of parameters density ratios of the order of 1×10^7 are achieved [12].

Fig. 3.4 shows the simulated coexistence curve for Kupershtokh model with van der Waals EOS and for $A = -0.152$ and $k = 0.01$. For this curve, a 2D spherical droplet ($R = 40$ [lu]) was initialized in the center of a rectangular domain (144×144 [lu]) and the temperature was varied through the simulation. Fig 3.5 shows that the density ratio ρ_l/ρ_v increases as the temperature $\bar{T}$ decreases. In inkjet printing applications, the density ratio is of the order of 1×10^3. In our simulations, this density ratio is achieved for temperatures around $\bar{T} = 0.3$. In addition to the density ratio, surface tension is a key parameter to describe the behavior of liquid jetting. The next section describes the procedure to estimate the surface tension in our simulations.

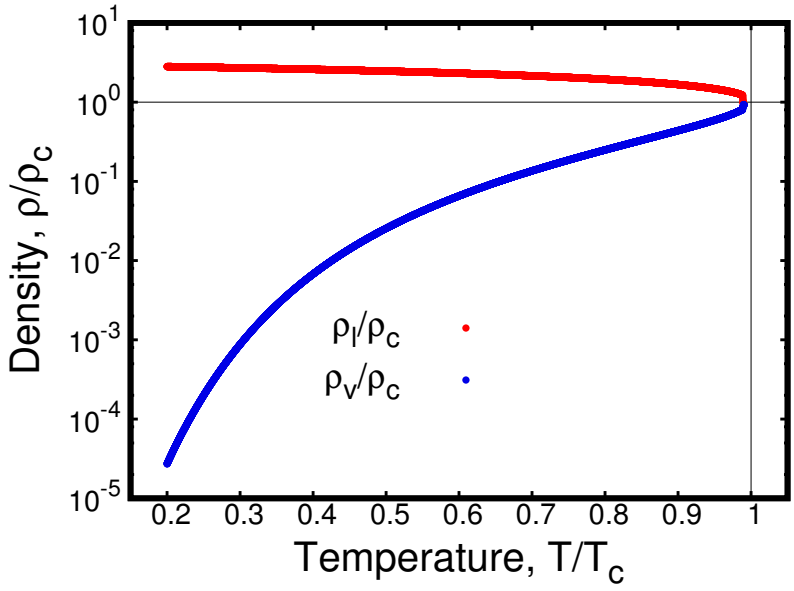

Figure 3.4: Liquid-vapor coexistence curve for kupershtokh multiphase model with van der Waals equation of state. Liquid $\bar{\rho}_l$ and vapor $\bar{\rho}_v$ densities are plotted as a function of the reduced temperature $\bar{T}$. The value of the parameters are: $A = -0.152$ and $k = 0.01$. In this simulation, a 2D spherical droplet with $R = 40$ [lu] was initialized in the center of a rectangular domain with dimensions of 144×144 [lu].

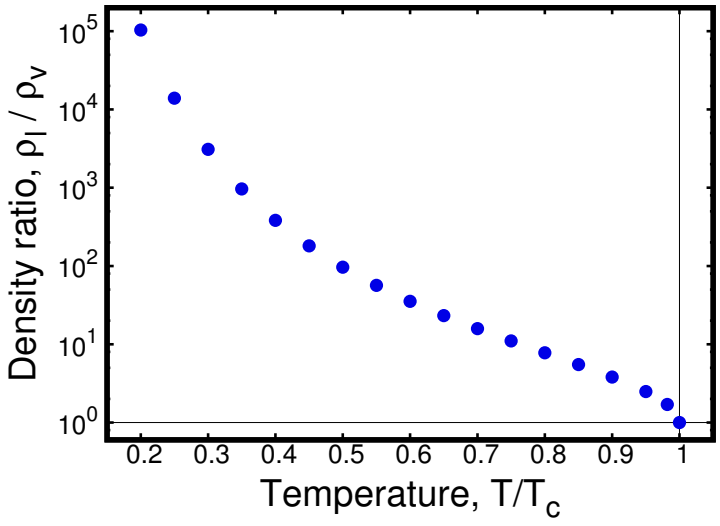

Figure 3.5: Liquid-vapor density ratio $\bar{\rho}_l/\bar{\rho}_v$ as a function of the temperature $\bar{T}$. This density ratio corresponds to the phase diagram presented in Fig. 3.5 The density ratio required for inkjet printing is of the order of $\rho_l/\rho_v \sim 1 \times 10^3$. In this plot the desired density ratio was achieved for temperatures $\bar{T} < 0.4$.

3.5 Estimating surface tension

The Laplace equation (Eq. 2.34) can be used to estimate the surface tension in our simulations. For this task, a set of droplets of different radius R are simulated. To calculate the surface tension, γ, the difference in capillary pressure ΔP inside and outside each droplet has to be measured. The

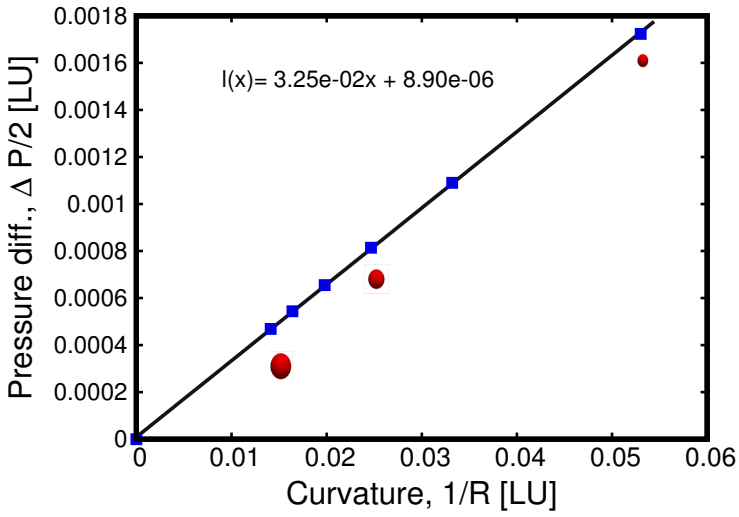

Figure 3.6: Plot of curvature of the droplets $1/R$ vs pressure difference inside and outside the droplets $\Delta P/2$. The slope of the linear fit gives the value of the surface tension $\gamma = 3.25 \times 10^{-2}$ [lu mu ts^{-2}]. In the simulations, the parameters are: $k = 0.01$, $\bar{T} = 0.7$, and the radius R were varied from 20 to 70 [lu]. In this plot, the red droplets illustrate the relative sizes of the droplets for each point.

radius R of the droplet can be estimated as follows [14]:

$$R_D = \left(\frac{M - N_x N_y \rho_v}{\pi(\rho_l - \rho_v)} \right)^{1/2} \tag{3.21}$$

where M is the total mass of the system, and N_x and N_y the size of the domain in X and Y directions, respectively. The capillary pressure ΔP can be obtained by measuring the densities inside ρ_l and outside of the droplet ρ_v and converting them to pressure P via the EOS. Once R and ΔP are measured, the slope of the plot $1/R$ vs $\Delta P/2$ gives the surface tension, see Eq. 2.34. Fig. 3.6 shows results for a set of droplets, yielding a surface tension $\gamma = 3.25 \times 10^{-2}$ [lu mu ts^{-2}]. The Kupershtokh parameters in this simulation are $k = 0.01$, $\bar{T} = 0.7$, and the radius R of the droplets was varied from $20 - 70$ [lu].

One minor drawback of our numerical scheme is that there is a coupling between density ratio ρ_l/ρ_v and surface tension γ. As shown in Fig. 3.7, surface tension γ increases as temperature $\bar{T}$ decreases. From Fig 3.5 and Fig. 3.7 this implies γ increases along with the density ratio ρ_l/ρ_v. In addition, Fig. 3.7 shows 2D images of a droplet at two different temperatures. From these images, we can see that the thickness of the liquid-vapor interface decreases as the surface tension increases. In the next section we present the modeling of the wetting conditions.

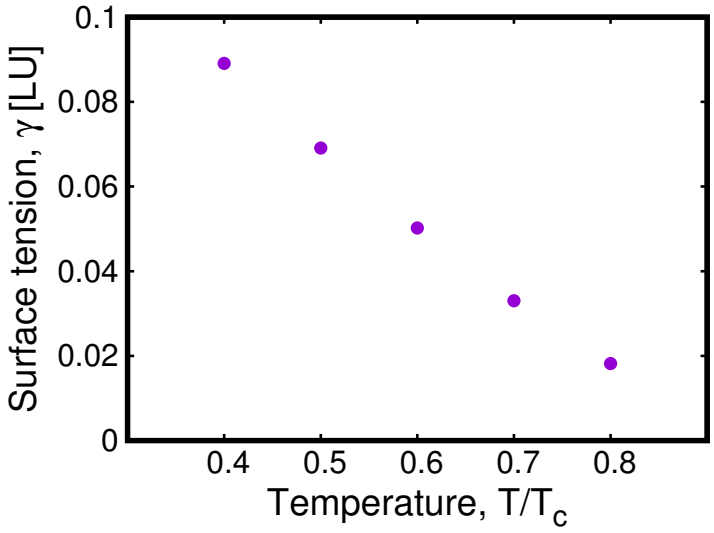

Figure 3.7: Plot of surface tension γ of a 2D droplet vs temperature $\bar{T}$. In our simulations, the surface tension γ and density ratio ρ_l/ρ_v increases as temperature decreases, see Fig. 3.5.

3.6 Modeling of the wetting conditions

In multiphase LBM, wetting conditions between fluids and solid surfaces can be modeled by incorporating an adhesive force between fluid and solid nodes [19]. Lets consider a solid node that interacts with a fluid node which has a density ρ_n. If the density of the fluid node is imposed at the solid node, it leads to a zero gradient of pressure between these two nodes i.e. a neutral wetting condition with a contact angle equal to 90 degrees. To impose a different wetting condition, we mirror the density and then we modify the value of the pseudopotential Φ when the fluid node interacts with the solid node. In this case, the pseudopotential Φ_w which accounts for the wetting conditions is

$$\Phi_w = \Phi - w \tag{3.22}$$

where the parameter w controls the wetting conditions and is a free parameter in our simulations. The wetting conditions imposed by the choice of w can be quantified by measuring the contact angle of a droplet sitting on a solid surface. The procedure for measuring the contact angles is described in the following section 3.7. The results of the simulated contact angles are presented in section 3.8.

3.7 Geometrical determination of contact angles (CA)

In order to determine the contact angles, the surface of the liquid phase must be located within the liquid-gas interface. As shown in Fig 3.7, this interface is a thin transition layer of fine width where the density changes smoothly. The droplet surface is defined as a set of points, each one of which connects a gas node and a liquid node. A gas node is defined as a node that has a density smaller than the mean density. A liquid node has density greater than the mean density. The mean density is defined as follows

$$\rho_m = \frac{\rho_l + \rho_v}{2} \tag{3.23}$$

where ρ_l and ρ_v are the liquid and vapor densities, respectively. Fig 3.8 illustrates the procedure for finding the surface of a liquid droplet. For this example, a droplet is situated in the center of a rectangular domain. To find the surface of the droplet, the density in the center of the domain is plotted as a function of the Y coordinate. From this plot, the points that belongs to the liquid surface are estimated, and the radius of the droplet calculated.

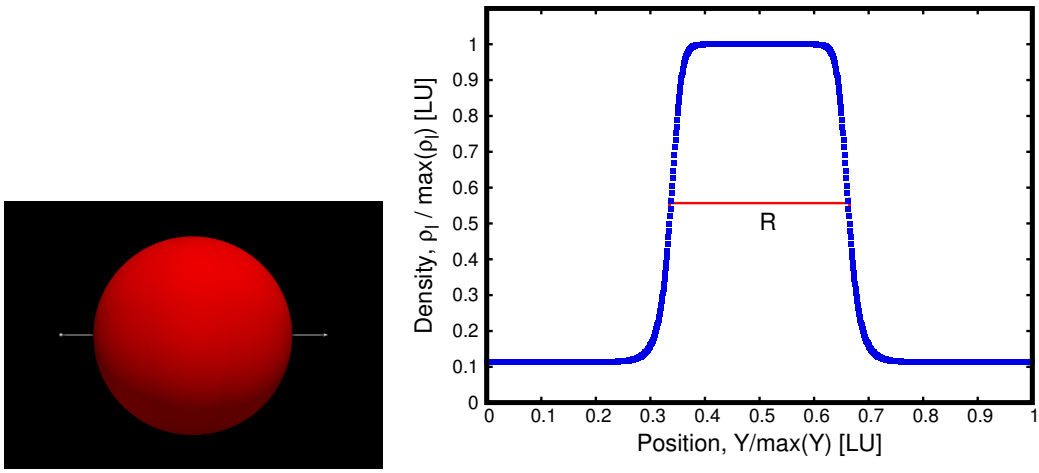

Figure 3.8: Illustration of the procedure used to find the surface of a droplet. Left panel: image of a spherical droplet in the center of a rectangular domain. Right panel: one dimensional plot for the density ρ of the droplet presented in the right panel, as a function of the position along a line parallel to the Y-axis.

Now that the droplet interface can be located, the contact angle θ can be estimated. This estimation is based on a geometrical approach [15] in which the sessile droplet is assumed to be a perfect spherical segment. From this spherical segment, the base b, height h and radius r have to be measured and the contact angle θ is estimated as follows

$$\theta = \pi - \arctan\left[\frac{b/2}{r-h}\right] \tag{3.24}$$

Fig 3.9 shows a graphical description of the geometrical approach for the estimation of contact angles. In our simulation,the base b of the sessile droplet was measured at a distance of two nodes

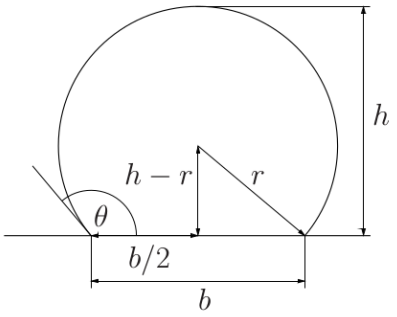

Figure 3.9: Geometrical determination of contact angle, figure reproduced from [15].

from the solid wall, and the height h was measured at the center of the droplet.

3.8 Contact angles as a function of the wetting parameter

The plot showed in Fig. 3.10 demonstrates that different contact angles can be obtained by adjusting the wetting parameter w. When the parameter w varies between -0.04 to 0.04 the contact angle varies from $\theta = 36$ to $\theta = 151$, respectively. In these simulations the domain is $144 \times 384 \times 384$

[LU], the upper and lower boundaries are solid walls, and the east and west boundaries are periodic. Here The vdW EOS is used with $k = 0.01$, $\bar{T} = 0.08$, and the liquid density $\rho_l = 1.95345$ and the vapor density $\rho_v = 0.261737$. For the simulations, a spherical 3D droplet of radius $R = 40$ [LU] is initialized in contact with the solid wall.

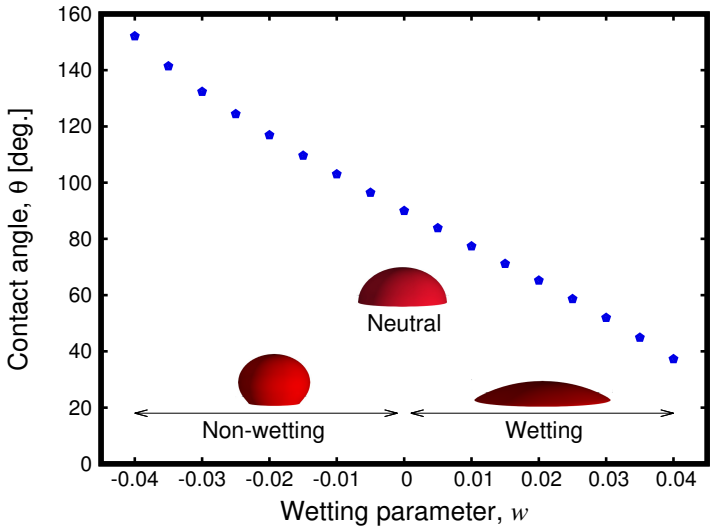

Figure 3.10: Contact angles for a fluid interacting with a surface as a function of the control parameter w. Simulation domain is $144 \times 384 \times 384$ with solid walls in the upper-lower boundaries and periodic in the east-west boundaries. A droplet with $R = 40$ [lu] is initially in contact with the solid wall; it is simulated till equilibrium is reached. The red droplets represent the regions of wetting, non-wetting and neutral wetting conditions.

Fig 3.11 shows fully 3D droplets with wetting, neutral and non-wetting contact angles. In these images, from left to right $w_1 = 0.04$, $\theta_1 = 36$; $w_2 = 0.00$, $\theta_2 = 90$; and $w_3 = -0.04$, $\theta_3 = 151$.

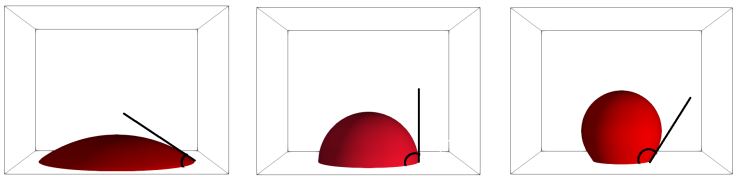

Figure 3.11: Simulation of 3D droplets wetting, neutral, and non-wetting contact angles. These wetting conditions are obtained by the force balance controlled by the parameter w. For this simulation $w_1 = 0.04$, $\theta_1 = 36$; $w2 = 0.00$, $\theta_2 = 90$; and $w3 = -0.04$, $\theta_3 = 151$.

In this chapter we reviewed the necessary concepts that allow us to use the multiphase Lattice Boltzmann method for the simulations of liquid jetting. With this numerical model we performed the simulations that are presented in the next chapter.

Chapter 4

Numerical simulations

In the previous chapters, we presented the theoretical and numerical framework of our multiphase numerical model. Our model, in principle, is able to simulate density ratios of the order of 1×10^7. *In this model we can easily impose open, periodic, and no-slip boundary conditions in complex geometries; in addition, in this model we can accurately control the wetting conditions in our simulations. Now we have the necessary framework to simulate fully 3D liquid jetting and to study the role of nozzle wettabilitty in the liquid jetting. In this chapter, we present our results for the 3D simulations. First, the geometry of the system is introduced in section 4.1. Second, a non-dimensional analysis of the problem is presented in section 4.2. Third, an estimation of the LB parameters is performed in section 4.3. Finally, we present results of the fully 3D simulations and the role of nozzle wettability on liquid jetting (section 4.4 and 4.5).*

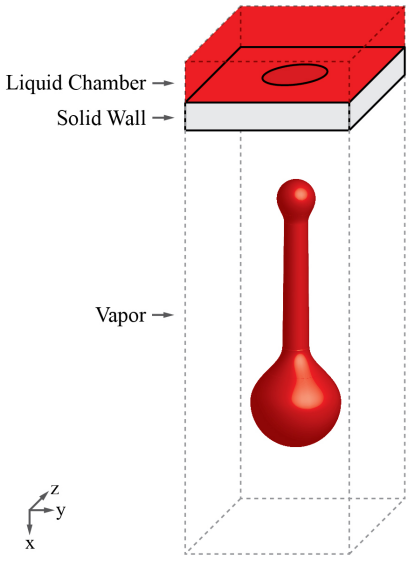

Figure 4.1: *Schematic representation of the 3D nozzle geometry. In the computational domain every node is either a fluid node or a solid node. This model has a liquid chamber (fluid), nozzle (solid) and vapor channel (fluid). For the boundary conditions: upper and lower are open, east-west and front-back are peridodic, and no-slip in the nozzle.*

4.1 Nozzle geometry

Fig. 4.1 shows a schematic view of the 3D nozzle geometry. In the computational domain every lattice node is either a fluid node (liquid and vapor chambers) or a solid node (nozzle). In the nozzle the bounceback algorithm is applied to mimic a non-slip boundary condition. The boundary conditions in our model are: upper and lower are open, and east-west and front-back are periodic. Fig. 4.2 shows the relevant parameters of the geometry. They are radius of the nozzle (R_n), velocity of the liquid at the nozzle (U_n), width of the chamber (R_c) and length of the channel (H). With these parameters and the properties of the liquid, we can calculate the non-dimensional groups of the system, and then we can estimate the Lattice Boltzmann parameters to make our simulations analogous to reality.

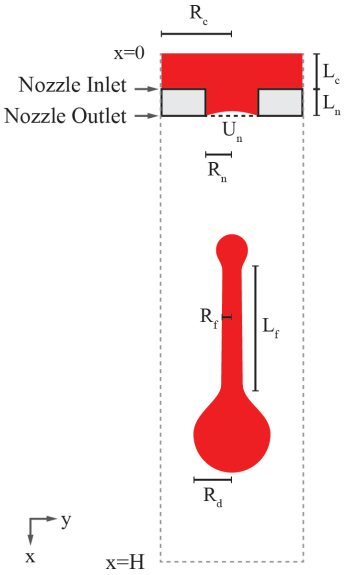

Figure 4.2: Image of a 2D slice of the domain. The relevant parameters of the geometry are: nozzle radius R_n, velocity of the liquid at the nozzle outlet U_n, width of the chamber R_c, and axial-length of the channel H.

4.2 Non-dimensional groups in inkjet printing

Surface tension, inertia, and viscosity can be used to describe the behavior of liquid jetting. To characterize the relative importance of these quantities we introduce the Reynolds (Re) and Weber (We) numbers as follows:

$$Re = \frac{\rho_l U_n R_n}{\mu}, \qquad We = \frac{\rho_l U_n^2 R_n}{\gamma} \tag{4.1}$$

where ρ_l is the density of the liquid, U_n its velocity at the nozzle outlet, μ its dynamic viscosity, R_n is the radius of the nozzle, and γ is the surface tension. Additionally, a third non-dimensional number, the Ohnesorge number (Oh) describes the ratio between surface tension and viscosity:

$$Oh = \frac{\sqrt{We}}{Re} = \frac{\mu}{\sqrt{\rho_l \gamma R_n}} \tag{4.2}$$

For optimal printing conditions the liquid jetting should have enough kinetic energy to eject from the nozzle, overcoming surface and viscous forces, characterized by We and Re. In addition,

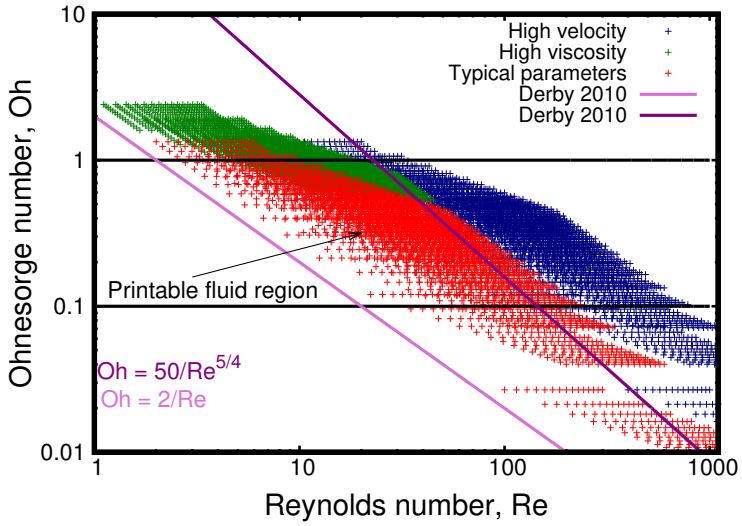

Figure 4.3: Non-dimensional parameter space map. It is suggested that stable operation regime of DoD printing is quoted by the black and pink lines, which represent pair of values of Ohnesorge and Reynolds numbers [9] [2]. Each color points on the plot represent a DoD inkjet system, which belongs to different regimes such as typical parameters in red color, high velocities, plotted in blue, and high viscosities, plotted in green. The values of these parameters are shown in Table 4.1.

optimal liquid jetting avoids satellite droplets and splashing onto the substrate, characterized by Oh. It is suggested in [2] that if $Oh > 1$, viscous forces will prevent jetting. On the other hand, if $Oh < 0.1$, surface forces dominate resulting in large number of satellite droplets [2]. It is also suggested in [9] that liquids can be optimally printed if Oh and Re follow the relations:

$$Oh > 50/Re^{5/4}, \qquad Oh < 2/Re \tag{4.3}$$

These four suggested inequalities for Oh define a region called the printable fluid region [2]. This region is shown in Fig. 4.3 enclosed by the black and purple lines. Fig. 4.3 also contains color points which represent the Re and Oh numbers for various inkjet printing systems. The red points represent real DoD inkjet printing systems [9]. The blue and green points represent hypothetical printing systems with relatively high velocity (high Re), and high viscosity (high Oh), respectively. This parameter space map offers a useful guide for selecting the physical properties of the domain and the liquid for our simulations.

Additionally to the Re, We, and Oh numbers, we need to consider a fourth non-dimensional number that represents the pressure pulse that drives the liquid jetting. This pressure difference across the nozzle and the resulting inertia of the liquid are time-dependent. In order to jet the liquid, the transient inertia must overcome surface and viscous forces. To characterize the relative importance between these forces the Womersley [16] (Wo) number is introduced:

$$Wo = R_n \sqrt{\frac{2\pi\omega}{\nu}} \tag{4.4}$$

where the angular frequency ω is the reciprocal value of the characteristic time scale of the problem. The modeling of the pressure pulse is presented in the next section.

4.2.1 Velocity pulse in the nozzle

We model the pressure pulse as a time-dependent velocity (inflow) boundary condition defined as follows:

$$U_n(t) = U_{n-max} \exp[-\xi^2 t^2] \cos[\omega t] \tag{4.5}$$

Parameter	Symbol	Value	SI units
Density of liquid	ρ_l	1.0 $\times 10^3$	[kg m^{-3}]
Radius of nozzle	R_n	10.0 - 70.0 $\times 10^{-6}$	[m]
Velocity at the nozzle	U_n	5.0 - 15.0	[m s^{-1}]
Surface tension	γ	20.0 - 70.0 $\times 10^{-3}$	[kg s^{-2}]
Viscosity	μ_l	1.0 - 50.0 $\times 10^{-3}$	[kg m^{-1} s^{-1}]
High viscosity	μ_l	60.0 - 90.0 $\times 10^{-3}$	[kg m^{-1} s^{-1}]
High velocity at the nozzle	U_n	20.0 - 60.0	[m s^{-1}]
Small radius of nozzle	R_n	1.0 - 10.0 $\times 10^{-6}$	[m]

Table 4.1: Set of parameters in SI for different DoD inkjet printing systems. Combinations of these parameters are plotted in the non-dimensional parameter space in Fig. 4.3.

where U_{n-max} is the maximum velocity at the nozzle, ω is the frequency, and ξ is a constant that controls the damping of the pulse. A typical velocity pulse from our simulations is plotted in Fig. 4.4, for $U_{n-max} = 9$ [m/s], $\xi = 1.87 \times 10^4$ [1/s], and $\omega = 1.04 \times 10^5$ [1/s].

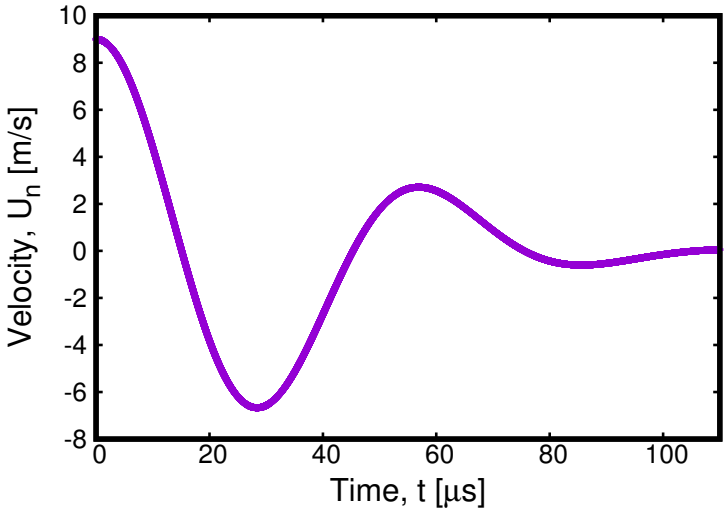

Figure 4.4: Plot of the velocity pulse given by Eq. 4.5. In this plot, the parameters in SI units are: $U_{n-max} = 9$ [m/s], $\xi = 1.87 \times 10^4$ [1/s], and $\omega = 1.04 \times 10^5$ [1/s].

In the last two sections the non-dimensional groups Oh, Re, We and Wo were introduced. Based on these numbers, the Lattice Boltzmann parameters for our simulations are estimated in the next section 4.3.

4.3 Estimation of the Lattice Boltzmann parameters

To simulate the flow conditions in the nozzle of a real inkjet printer the Oh, Re, We and Wo numbers should be identical in both the simulation and reality. This presents some challenges for our numerical model. There is a restriction on the maximum velocity in the system due to the fact that LBM provides a solution for flows only in the incompressible regime [19] [16] [17]. Further, there is also a restriction on the size of the computational domain, which is related to the computational infrastructure available. Finally, our numerical model has a coupling between density ratio and surface tension, as shown in section 3.5. As a result, the estimation of the LB parameters for our simulation is a delicate task. Based on the practical knowledge of our system, to

calculate the LB parameters we consider a balance between the capabilities of our computational infrastructure, the real system we want to simulate, and the desire to get a high density ratio ($\rho_l/\rho_v \cong 2 \times 10^2$). We propose the following procedure for estimating the LB parameters:

1. obtain the parameters of an inkjet printer in SI units,
2. calculate the dimensionless numbers Oh, Re, We, and Wo, and
3. estimate the Lattice Boltzmann parameters as a function of the non-dimensional groups.

As an example of this estimation, let us consider the parameters in SI units presented in table 4.2. These parameters were found in [9].

Parameter	Value	SI units
R_n	15.00×10^{-6}	[m]
U_{n-max}	9.00	[m s^{-1}]
ρ_l	1.00×10^{3}	[kg m^{-3}]
ρ_v	4.67	[kg m^{-3}]
γ	8.00×10^{-2}	[kg s^{-2}]
μ_l	5.00×10^{-3}	[kg m^{-1} s^{-1}]
ω	1.04×10^{5}	[s^{-1}]

Table 4.2: Parameters in SI units of a real inkjet printer. The non-dimensional numbers for the system are: $Re = 27.00$, $We = 14.28$, $Oh = 0.14$, and $Wo = 5.44$. The Re and Oh numbers define a point inside the parameter space map, as shown by the red point in Fig. 4.5. This point lies inside the printable fluid region of the map.

The non-dimensional numbers for this system are: $Re_s = 27.00$, $We_s = 14.28$, $Oh_s = 0.14$ and $Wo_s = 5.44$. The values of Re_s and Oh_s define a point inside the printable fluid region of the map, as shown by the red point in Fig 4.5.

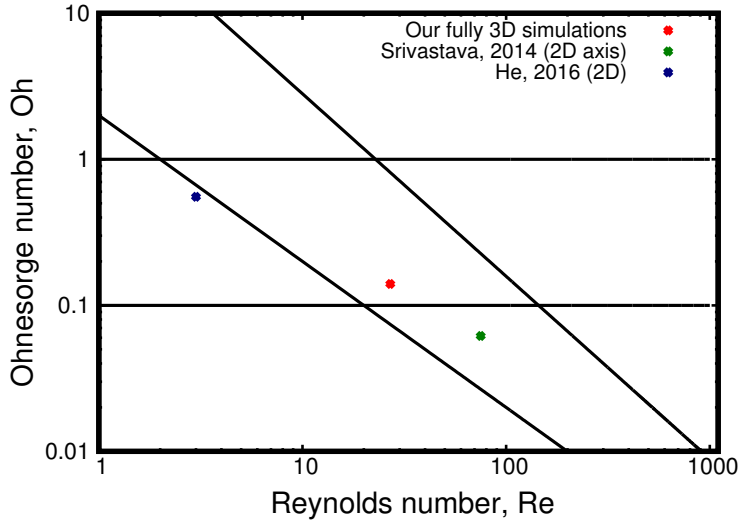

Figure 4.5: Space map for the Lattice Boltzmann simulations of liquid jetting. The red dot represents our fully 3D simulations, the blue dot is from a 2D simulation [7], and the green dot a 2D axisymmetric simulation [16].

Now, we need to find a set of LBM parameters that match the Re_s and We_s numbers:

$$We_s = \frac{\rho_l U_n^2 R_n}{\gamma}, \qquad Re_s = \frac{U_n R_n}{\nu} \tag{4.6}$$

For We_s, the temperature $\bar{T}$ of the system defines the density ρ_l and surface tension γ. Therefore, the velocity U_n can be expressed as a function of R_n as follows

$$U_n = \sqrt{\frac{\gamma We_s}{\rho_l}} \frac{1}{\sqrt{R_n}} = \Pi \frac{1}{\sqrt{R_n}} \tag{4.7}$$

where $\Pi = \Pi(\bar{T})$ is a constant, Fig. 4.6 shows the contour lines for $\bar{T} = 0.4$ and $\bar{T} = 0.8$.
For Re_s, the relaxation parameter $\tau = \frac{1}{2} + \frac{\nu}{c_s^2}$ gives the kinematic viscosity ν, analogously the velocity U_n is expressed as a function of R_n as follows

$$U_n = \nu Re_s \frac{1}{R_n} = Z \frac{1}{R_n} \tag{4.8}$$

where $Z = Z(\tau)$, Fig. 4.6 shows the contour lines for $\tau = 0.9$ and $\tau = 1.3$.

The region enclosed by the contour lines of We_s and Re_s gives the appropriate values of R_n and U_n for the Lattice Boltzmann simulations. Note that the velocity in our system has to be $U_n < 0.1$ due to the incompressibility of our method. In the next section a procedure for converting Lattice Boltzmann units to SI units and viceversa is presented.

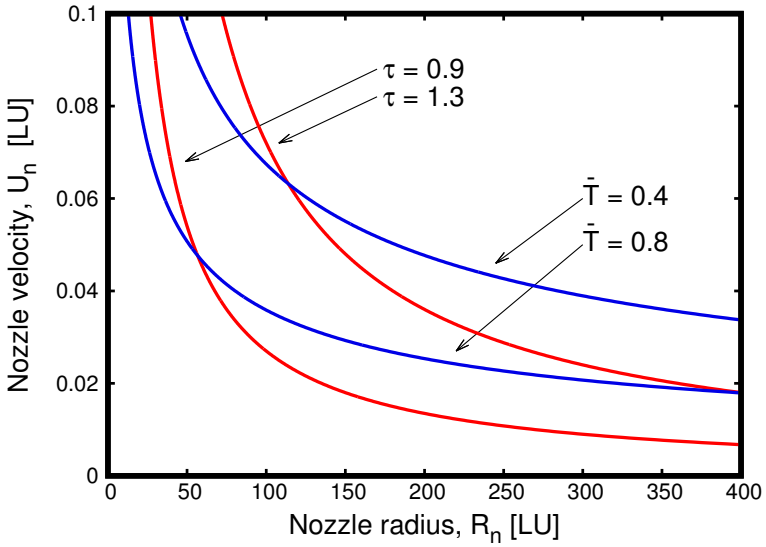

Figure 4.6: Phase diagram for selection of LBM parameters. This plot represents a system with $Re = 27$, $Oh = 0.14$, and $Wo = 5.44$. The enclosed region between red and blue lines represent LB systems that match the non-dimensional numbers. Each point in the enclosed region has a unique value of U_n, R_n, τ, and $\bar{T}$

.

4.3.1 Unit conversion

This research is focused on industrial applications of inkjet printing. For this reason, it is desired to express all the quantities of our simulations in the international system of units, SI units. Here we present the procedure proposed in [16] to convert the parameters from Lattice Boltzmann units (LU) to SI units. For this task, only three basic dimensions are considered: mass $[M]$, length $[L]$, and time $[T]$. Any physical quantity in the system can be expressed as a product of these basic quantities as follows

$$[q] = M^{\alpha} L^{\beta} T^{\delta} \tag{4.9}$$

In the inkjet system, the characteristic length, mass and time scales are: R_n, $\rho_l R_n^3$, and ω^{-1}, respectively. With these scales any physical quantity q can be non-dimensionalized as follows

$$q* = \frac{q}{(\rho_l)^{\alpha}(R_n)^{3\alpha+\beta}(\omega)^{-\delta}} \tag{4.10}$$

where $q*$ is dimensionless and α, β and γ are determined by the dimensions of q.

For the system presented in table 4.2, the characteristic scales in SI units are: $U_n = 9 \quad [m/s]$, $R_n = 15 \quad [\mu m]$, $\rho_l = 10^3 \quad [kg/m^3]$, $\gamma = 0.08 \quad [N/m]$, $\mu_l = 0.005 \quad [kg/m/s]$ and $\omega = 1.04 \times 10^5 \quad [Hz]$. For these quantities, the dimensionless groups are: $Re = 27.00$, $We = 14.28$, $Oh = 0.14$, and $Wo = 5.44$.

First, $\bar{T} = 0.43$, and $\tau = 1.00$, which leads to $R_n = 45$ and $U_n = 0.1$ in LU. The values of $\rho_l = 2.572$, $\rho_v = 0.012$, and γ were dictated by $\bar{T} = 0.43$. The density ratio is: $\rho_l/\rho_v = 214$. In addition, $\tau = 1$ in combination with the density gives $\mu_l = 0.428$. This set of parameters in combination with $Wo = 5.44$ gives us $\omega = 3.88 \times 10^{-4}$ in LU. Now, we use the phasediagram presented in Fig. 4.6

Finally, the rule presented in Eq. 4.10 is used to calculate the values of $q*$ for all the parameters. The table 4.3 present the results for the estimation of the LB parameters and the conversion factors between systems of units. In the next section, we present the simulations performed with this set of parameters.

q	LU	q*	SI (kg,m,s)	[q]
Δx	1.00	2.20×10^{-2}	3.30×10^{-7}	L
Δm	1.00	4.26×10^{-6}	1.44×10^{-18}	M
Δt	1.00	3.88×10^{-4}	3.73×10^{-9}	T
R_n	45	1.00	1.50×10^{-5}	L
R_c	240	5.33	7.99×10^{-5}	L
H	1104	24.53	3.67×10^{-4}	L
U_n	0.1	5.70	9.00	LT^{-1}
ρ_l	2.572	1.00	1.00×10^{3}	ML^{-3}
ρ_v	0.012	4.66×10^{-3}	4.67	ML^{-3}
γ	0.08	2.20	8.00×10^{-2}	MT^{-2}
μ_l	0.428	0.21	5.00×10^{-3}	$ML^{-1}T^{-1}$
ω	3.88×10^{-4}	1.0	1.04×10^{5}	T^{-1}
ξ	7.22×10^{-5}	0.18	1.87×10^{4}	T^{-1}

Table 4.3: Table for parameter conversion between LB, SI units and other simulation methods. The set of parameters correspond to the following dimensionless numbers: $Re = 27.00$, $Oh = 0.14$, and $Wo = 5.44$. The LB parameters: U_n, R_n, ρ_l, μ_l, γ, and ω where calculated with the phase diagram presented in Fig 4.6. The density ratio for LB is equal to 214. Fully 3D simulations for these parameters are shown in Fig. A.1.

4.4 Fully 3D numerical simulations of liquid jetting

In the previous chapters, we presented the theoretical framework and a detailed analysis of our multiphase numerical model. Now we are capable of performing fully 3D simulations of liquid jetting, and also capable of measuring the relevant parameters of the jetting, for example, densities, velocities, contact angles, isovolumes, and positions of the liquid droplets. The results of our simulations are presented here.

Fig. 4.7 shows qualitative numerical results of a 3D liquid jetting. This image shows a visualization of an isovolume of the density, which represents the liquid phase. The geometry used for this simulation is shown in Fig. 4.2 and the parameters in SI and LB units are presented in

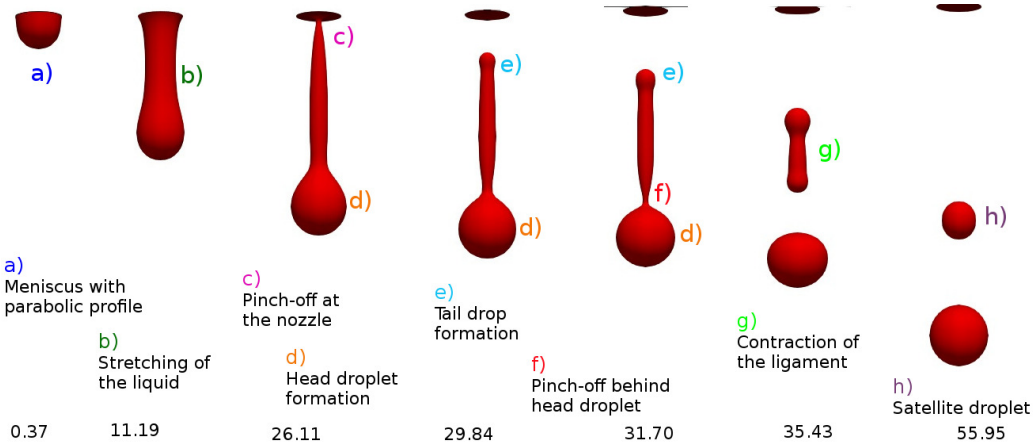

Figure 4.7: Qualitative numerical results of 3D liquid jetting. The red droplet is an isovolume of densities, $\rho_{iso} > \rho_m$, where ρ_m is defined in Eq. 3.23, therefore, the red droplet represents the liquid phase. The density ratio in this case is $\rho_l/\rho_v = 214$. Times are expressed in $[\mu s]$. From left to right we can observe: (a) meniscus, (b) stretching of the liquid, (c) pinch-off at the nozzle, (d) head droplet, (e) tail droplet, (f) pinch-off behind the head droplet, and (g,h) satellite droplet. The geometry and set of parameters for this simulation are shown in Fig. 4.2 and table 4.3, respectively. Time series of this drop formation are shown in Fig. A.1.

table 4.3. The density ratio in this simulation is $\rho_l/\rho_v = 214$. In this image we can observe the main stages of the drop formation process, which are summarized as follows:

In the initial stage ($t = 0.37 \quad [\mu s]$) the meniscus shows a typical parabolic profile. We can observe at $t = 11.19 \quad [\mu s]$ that the liquid is stretching due to surface tension effects. This stretching leads to the formation of the head droplet ($t = 11.19{-}31.70 \quad [\mu s]$). Next the pinch-off at the nozzle is observed at $t = 26.11 \quad [\mu s]$ and tail drop formation at $t = 29.84 \quad [\mu s]$. After the pinch-off at the nozzle, a second pinch-off takes place behind the head droplet ($t = 31.70 \quad [\mu s]$). This second pinch-off breaks the jet into two parts, a head droplet and a ligament ($t = 35.43 \quad [\mu s]$). In the last stage, the ligament contracts to form a secondary droplet, a satellite droplet ($t = 55.95 \quad [\mu s]$). A complete time series of this drop formation is showed in Fig. A.1. From the simulations, we can also obtain information about particular points inside the liquid region, for example the positions and velocities of the head droplet, tail droplet, and tip of the tail.

Fig. 4.8 shows plots for the positions and velocities as a function of time of the head droplet (c), tail droplet (a) and tip of the tail (b). To find the surface of the liquid jet, we used the algorithm presented in section 3.7, once the points are found, we can measure the velocity at these particular points. In the left panel, we can observe the time of pinch-off from the nozzle, and the time of pinch-off behind the head droplet. In addition, from the positions of (a) and (b) we can observe the contraction of the ligament into a satellite droplet.

In the right panel, the velocities of (a), (b) and (c) are plotted as a function of time. In this plot, one can observe the maximum velocity of the meniscus ($U \cong 9 \quad [m/s]$), which is imposed by the maximum velocity of the velocity pulse ($U_n = 9 \quad [m/s]$). In addition, we can observe that after some time, $t \cong 60 \quad [\mu s]$, both the main and satellite droplets reach a final common velocity, $U \cong 3.9 \quad [m/s]$. In this velocity plot (Fig. 4.8), we can also observe fluctuations between the velocity of the tail droplet (a) and the velocity of tip of the tail (c). It is observed that when the velocity of (a) is at a maximum, at the same time the velocity of (b) is at a minimum and vice versa.

To recapitulate, in this section, we have presented results of the 3D simulations of liquid jetting. This results qualitatively show that we have set up a computational tool that is capable of simulating the whole drop formation process in inkjet printing. In addition, our approach shows that we are able of measuring the relevant physical quantities in the system. To end this section,

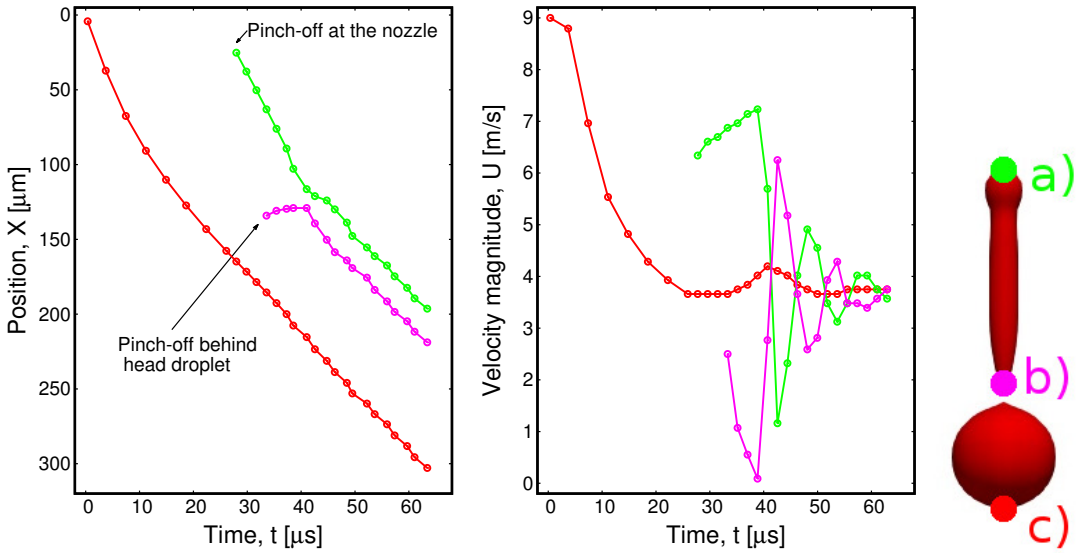

Figure 4.8: Left panel: position of the head droplet (c), tail droplet (a), and tip of the tail (b), as a function of time. The surface of the liquid jet was found with the algorithm presented in section 3.7. Right panel: velocity magnitude of (c), (a), and (b) as a function of time. In this image we can observe that initially the meniscus has a maximum velocity, $U \cong 9 \quad [m/s]$, imposed by the maximum velocity, $U_n = 9 \quad [m/s]$, of the velocity pulse; in addition, we can observe that both the main and head droplet reach a final common velocity, $U \cong 3.9 \quad [m/s]$. Fig. A.3 and Fig. A.2 show colorbar images of the velocity magnitude and isovolumes of the density of the jetting as a function of time, respectively.

we highlight three aspects that show the achievements of our simulations when compared with similar attempts ([16]) to simulate liquid jetting with the multiphase LBM: (i) our simulations have a higher density ratio 224 vs 10, (ii) our model is capable of simulating liquid jetting with parameters that lie inside the printable fluid region of the parameter space map (see section 4.2), and (iii) our simulations do not show numerical enhanced evaporation of the satellite droplets. Now that we are capable of perform the 3D simulations of liquid jetting, in the next section, we present a preliminary investigation of the role of nozzle wettability in the liquid jetting.

4.5 The role of nozzle wettability in the liquid jetting

The research topic presented here is motivated by experiments that have been carried at the laboratories in Océ technologies. These experiments suggest that structural defects in the nozzle, such as non-homogeneous wetting conditions, may play an adverse role on the liquid jetting. These defects could change, for example, the size and shape of the droplets, and could also deviate the jet from its axial trajectory. If these effects appear in a real inkjet printer, they could drastically compromise the quality of the printing. At this time, we have not found numerical investigations in this topic. We think that these investigations ideally must be performed in a 3D domain, because the undesired effects are in principle not axisymmetric.

In this context, we use our computational toolbox to perform a preliminary investigation of the role of non-symmetric wetting conditions in the nozzle. In this first study, we set up a simple case which simulates a nozzle that has a wetting condition in one half of it, and a different wetting condition in the other half. The 3D geometry for these simulations is shown in Fig. 4.1 and the configuration of the non-homogeneous wetting conditions is illustrated in Fig. 4.9. The non-symmetric wetting conditions in the nozzle are imposed by the wetting parameters w_1 and w_2. It results in two different contact angles in the nozzle, θ_1 in one half and θ_2 in the other half,

respectively.

Fig. 4.10 shows qualitative numerical results of a simulation with non-symmetric wetting conditions in the nozzle, where in one half $\theta_1 = 36$ and in the other half $\theta_2 = 151$. In this figure, we can see that the jetting shows a different shape as compared with a jetting ejected from a nozzle with symmetric wetting conditions. In addition, a similar comparison shows that the head droplet does not have a typical symmetric profile. The parameters in LB and SI units for these simulations are presented in table 4.4.

q	LU	SI	Units [q]
R_n	45	1.50×10^{-5}	L
R_c	288	7.99×10^{-5}	L
H	1440	3.67×10^{-4}	L
U_n	0.1	9.00	LT^{-1}
ρ_l	1.95345	1.00×10^{3}	ML^{-3}
ρ_v	0.261736	134	ML^{-3}
γ	0.017	2.30×10^{-2}	MT^{-2}
μ_l	0.428	6.50×10^{-3}	$ML^{-1}T^{-1}$
ω	3.88×10^{-4}	7.84×10^{5}	T^{-1}

Table 4.4: Table of parameters in LB and SI units for the simulations with non-homogeneous wetting conditions in the nozzle. The set of parameters correspond to the following dimensionless numbers: $Re = 20.50$, $We = 51.7$ and $Wo = 4.74$.

The non-symmetric wetting condition may also influence the contact line dynamics in the nozzle. Fig. 4.11 shows images of the contact line in the nozzle. In this image, we can observe that there exist two different contact lines in each half of the nozzle, and we can also observe that the liquid jetting pinches-off first on the side of the nozzle that has a non-wetting contact angle, $\theta_2 = 151$. This qualitative results illustrates the influence of the non-symmetric wetting conditions in the shape of the droplet and contact line.

Now we investigate if these conditions in the nozzle also deviate the liquid jetting from its axial trajectory. Fig. 4.9 illustrates this problem, where a droplet hypothetically deviates from its axial trajectory. For this task, we measure the trajectory of the center of mass of the jetting as a function of the non-symmetric wetting conditions in the nozzle. This center of mass is calculated from an isovolume of the density, which represents the liquid phase. This isovolume is defined as a set of points inside the domain, where each point has a density greater than the mean density defined in Eq. 3.23. Once the isovolume is calculated, we measure the center of mass of the liquid jetting as follows:

$$\boldsymbol{CM}(\boldsymbol{x}, t) = \frac{1}{M}\sum_{i=1}^{n} \rho_i \boldsymbol{x}_i, \qquad M = \sum_{i=1}^{n} \rho_i \tag{4.11}$$

where n is the number of points inside the isovolume, $\boldsymbol{x_i}$ and ρ_i are the position and the density at the point i, respectively, and t is the time. Note that computing the center of mass is a relatively demanding task, because our domain contains 119439360 nodes, and every node has its own density and positions.

Fig. 4.12 shows the trajectories of the center of mass of the jetting for different combinations of w_1 and w_2. In these set of simulations, we maintain half of the nozzle with a fixed wetting condition, $w_1 = 0.4$, which represents $\theta_1 = 36$. The value of w_2 will be varied from $w_2 = 0.4$ to $w_2 = -0.4$, which imposes contact angles from $\theta_2 = 36$ to $\theta_2 = 151$, respectively. The left panel shows the position of the center of mass in the center of the domain in a plane parallel to the Y axis. This is a 2D plot, because the center of mass does not deviate in the direction parallel to Z, see Fig. 4.9. In this plot, we can observe that the non-symmetric wetting conditions in the nozzle deviate the trajectories of the jetting in the direction paralel to Y. The plot also shows that by increasing the difference of contact angles, $\Delta\theta = |\theta_2 - \theta_1|$, the deviation, R_{dev}, increases. To estimate the value of the angle α and the deviation R_{dev}, we applied a linear fit to the trajectories.

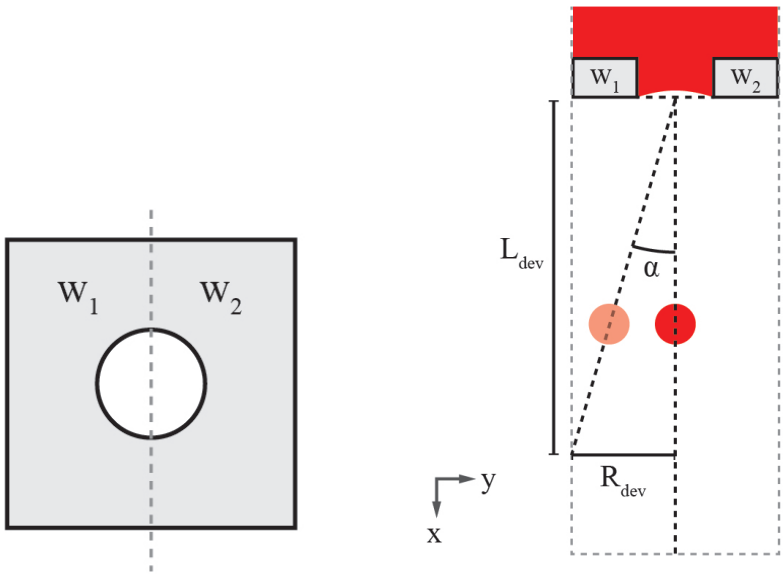

Figure 4.9: Left panel: Schematic top view of a nozzle plate with non-symmetric wetting conditions. The parameters w_1 and w_2 represent a particular wetting condition, θ_1 and θ_2, in the nozzle surface. Right panel: Side view of the 3D geometry. This image illustrates the deviation of the droplet from its perfect axial trajectory. The angle α and deviation distance R_{dev} depend on the combination of wetting conditions w_1 and w_2 on the nozzle.

From the linear fit, we calculated the deviation, R_{dev}, as a function of w_2, and for different lengths of the channel, L_{dev}. Fig. 4.12 shows these results of the deviation, R_{dev}, as a function of the wetting condition w_2 and for different lengths of the channel L_{dev}. It was found that for a channel of 2 $[mm]$ length, the center of mass of the droplet can deviate 25 $[\mu m]$, in the case of $\theta_1 = 36$ and $\theta_2 = 151$. Note that this deviation, R_{dev}, is equal to zero for the case of symmetric wetting conditions, $\Delta\theta = 0$, in the nozzle.

Now we calculate the Y velocity of the center of mass as a function of the wetting conditions. Fig. 4.13 shows a plot of the trajectories of this center of mass as a function of time. From this trajectories, we apply a linear fit to the tail of the plot to obtain the final velocity of the droplet, U. This final velocity of the center of mass increase as $\Delta\theta = \theta_2 - \theta_1$ increases. It implies that by increasing the value of $\Delta\theta$, the liquid jetting acquire a higher momentum in Y direction. For a nozzle with symmetric wetting conditions, this velocity is equal to zero.

In this section, we applied our computational tool to study the role of non-symmetric wetting conditions in the nozzle. The results have shown that these conditions modify the shape and symmetric profile of the liquid droplets, and ligaments. It was also found that these conditions lead to two different contact lines in each half of the nozzle. Finally, the results have shown that these non-symmetric wetting conditions deviate the liquid jetting from its perfect axial trajectory.

In the next section, we briefly discuss some conclusions of this thesis.

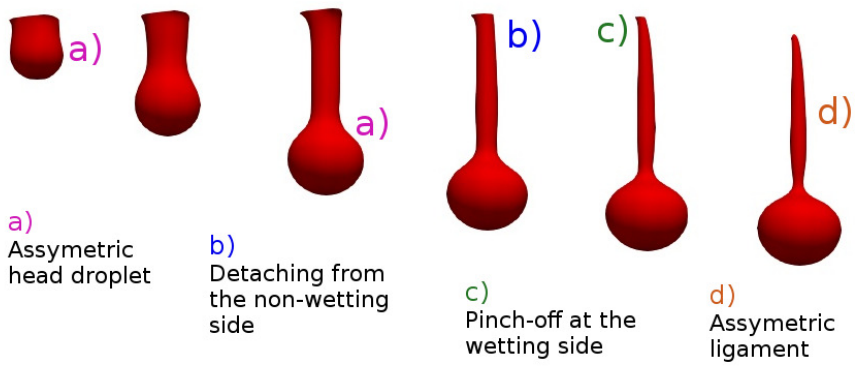

Figure 4.10: Qualitative numerical results of the simulations with non-symmetric wetting conditions in the nozzle. In this image, we can observe the effects of these wetting conditions, which result in changes in the typical dynamics and shape of the droplet and ligament. In this simulation, the left side of the nozzle has $w_1 = 0.4$, and the right side has $w_2 = -0.4$, with $\theta_1 = 36$ and $\theta_2 = 151$, respectively. The parameters of this simulation are shown in table 4.4.

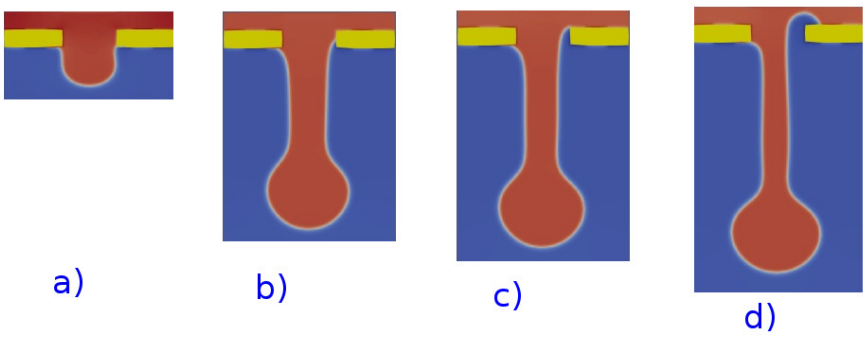

Figure 4.11: Images of a 2D slice in the center of the domain, where red is the liquid phase. This figure shows that the non-symmetric wetting conditions result in two different contact lines in each half of the nozzle. The left side of the nozzle refers to a contact angle $\theta_1 = 36$, and the right side to $\theta_2 = 151$. In images a) and b), we can observe that there exist two different contact lines in each half of the nozzle. In images c) and d), we can observe that the liquid pinches-off first on the right side.

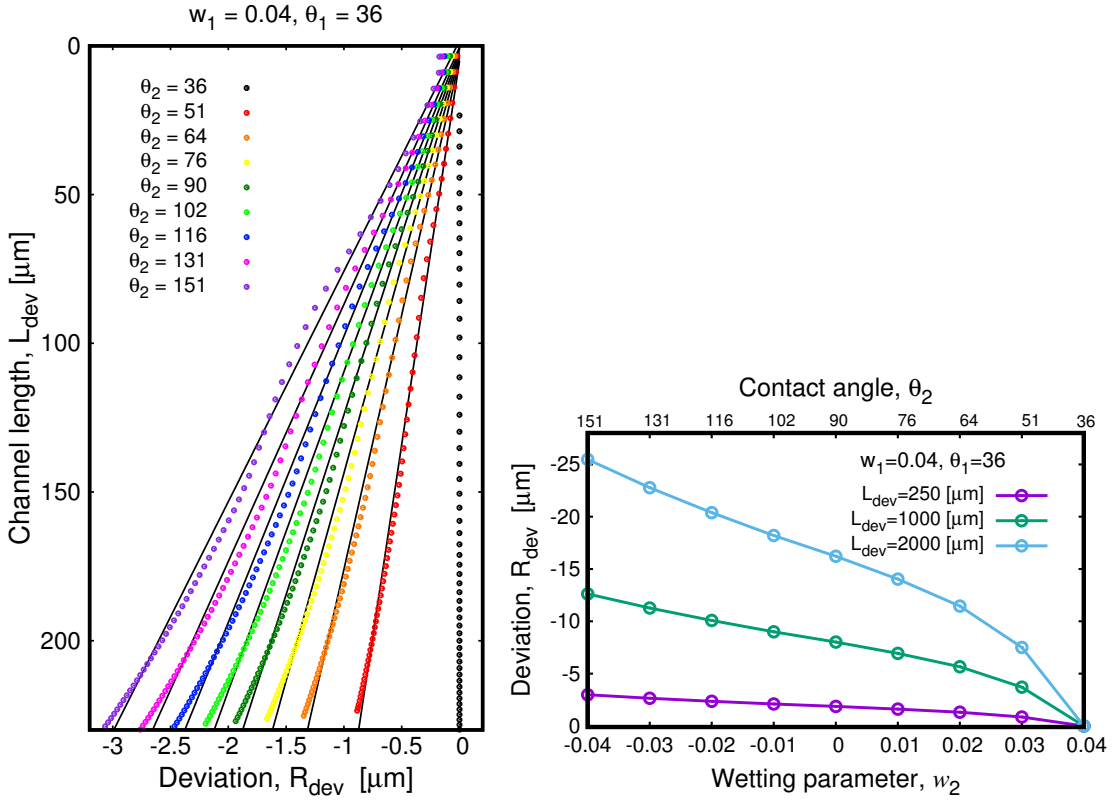

Figure 4.12: Left panel: Position of the center of mass of the liquid jetting. The jet deviates in the Y direction. It is a 2D plot, because the center of mass has a perfect axial trajectory in the Z direction (see Fig.4.9). In this plot, $w_1 = 0.04$ and $\theta_1 = 36$, and the values of θ_2 were varied from $\theta_2 = 36$ to $\theta_2 = 151$. The black lines represent a linear fit, which is used to calculate the value of the deviation R_{dev}. Right panel: shows the calculations of the deviation R_{dev} for different wetting conditions, $\Delta\theta = \theta_2 - \theta_1$, and for different channel lengths, L_{dev}.

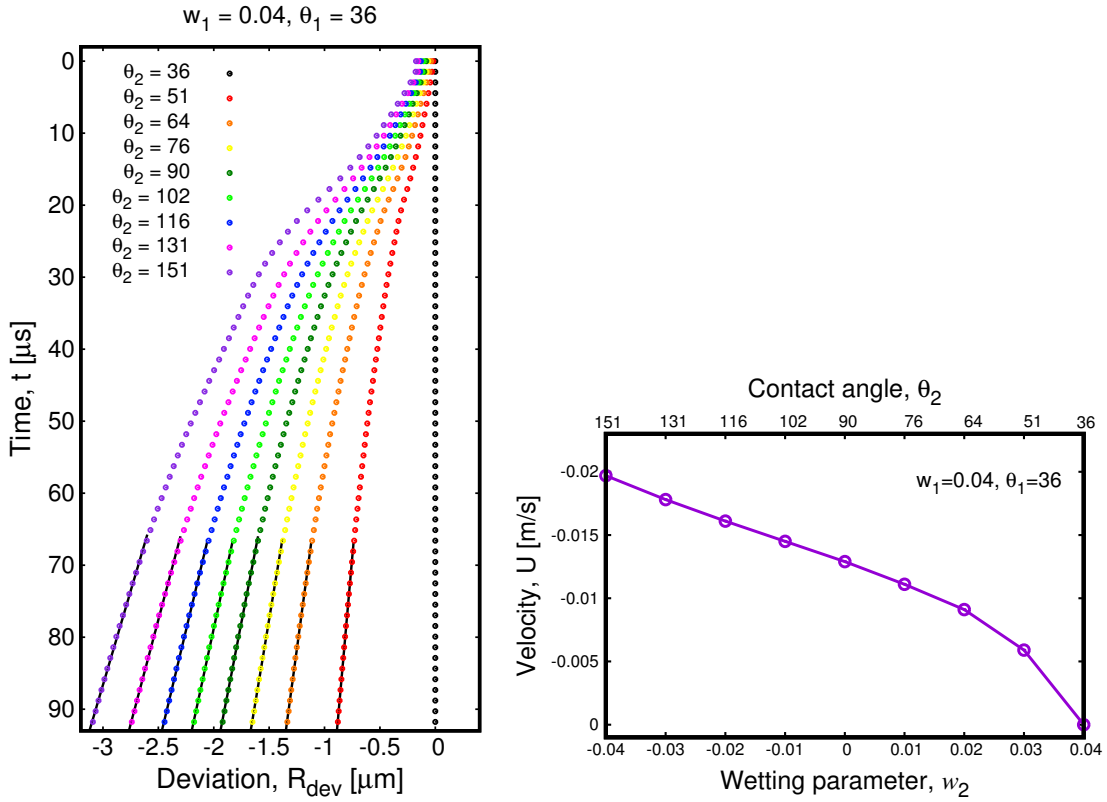

Figure 4.13: Left panel: Plot of the Y coordinate of the center of mass of the jetting as a function of time. The value of $\theta_1 = 36$ and θ_2 is varied from $\theta_2 = 36$ to $\theta_2 = 151$. In this plot, a linear fit of the tail of the plot gives us the value of the velocity, U, of the droplet. Right panel: the values of the final velocity, U, are plotted for different wetting conditions.

Chapter 5

Conclusions

In this report, we have shown how to numerically simulate liquid jetting in inkjet printing by using the multiphase Lattice Boltzmann method. We found that the Kupershtokh LB method is a viable tool for performing fully 3D simulations of real liquid jetting under some restrictions on Re, We, and Wo, and a restriction on the density ratio between the liquid and vapor phase, ρ_l/ρ_v. Many of the conditions encountered are intrinsic to the Kupershtokh model and not to LBM in general.

The results of the simulations qualitatively show that our approach is capable to simulate the whole drop formation process of the liquid jetting. We also show that the relevant physical quantities of the system can be quantitatively measure in the simulations. In this simulations, we were able to obtain a density ratio of the order of 2×10^2, and also able to overcome the numerical enhanced evaporation that other multiphase LBM models have shown.

Furthermore, we applied our computational tool to study structural deffects in the nozzle, particularly, the role of non-symmetric wetting conditions in the nozzle. We found that this non-symmetric wetting conditions can change the typical shape, and symmetric profile of the liquid jetting. In addition, it was found that this conditions can deviate the jetting from its axial trajectory. It was found that by increasing the difference in contact angles, $\Delta\theta = \theta_2 - \theta_1$, the deviation from the axial trajectory, R_{dev}, increases.

Finally, further improvements in the approach are necessary in order for it to become a more useful and quantitative computational tool. The major remaining issues include: (1) further enhancement of numerical stability to achieve higher density ratios; (2) further improvements of the numerical scheme in order to decouple density ratio and surface tension; (3) including a more realistic pressure pulse and the acoustic dynamics in the nozzle chamber; (4) and direct comparison with experimental or other numerical results.

Bibliography

[1] Prof. Anton Darhuber. *Microfluidics and nanofluidics notes*. 2015. 11

[2] Brian Derby. Inkjet printing of functional and structural materials: Fluid property requirements, feature stability, and resolution. *Annu. Rev. Mater. Res.*, 40:395–414, 2010. 26

[3] Theo Driessen and Roger Jeurissen. A regularised one-dimensional drop formation and coalescence model using a total variation diminishing (tvd) scheme on a single eulerian grid. *International Journal of Computational Fluid Dynamics*, 25(6):333–343, 2011. 3

[4] Theo Driessen and Roger Jeurissen. *Drop Formation in Inkjet Printing*, pages 93–116. Wiley-VCH Verlag GmbH & Co. KGaA, 2016. 1, 2, 3

[5] Theodorus Wilhelmus Driessen. *Drop formation from axi-symmetric fluid jets*. PhD thesis, Universiteit Twente, 2013. 1, 3

[6] National geographic. Water strider, 2017. 11

[7] Bing He, Sucui Yang, Zhangrong Qin, Binghai Wen, and Chaoying Zhang. The roles of wettability and surface tension in droplet formation during inkjet printing. *arXiv preprint arXiv:1702.04487*, 2017. 3, 17, 28

[8] H. Huang, M. Sukop, and X. Lu. *Multiphase Lattice Boltzmann Methods: Theory and Application*. Wiley, 2015. 3, 7, 17

[9] Ian M. Hutchings, Graham D. Martin, and Stephen D. Hoath. *Introductory Remarks*. Wiley-VCH Verlag GmbH Co. KGaA, 2016. 1, 2, 26, 28

[10] R. J. M. Jeurissen. *Bubbles in inkjet printheads: analytical and numerical models*. PhD thesis, Universiteit Twente, 2009. 3

[11] Timm Krueger, Halim Kusumaatmaja, Alexandr Kuzmin, Orest Shardt, Goncalo Silva, and Erlend Magnus Viggen. *The Lattice Boltzmann Method: Principles and Practice*. Graduate Texts in Physics. Springer, 2016. 6, 7, 8, 9, 10

[12] A.L. Kupershtokh, D.A. Medvedev, and D.I. Karpov. On equations of state in a lattice boltzmann method. *Computers & Mathematics with Applications*, 58(5):965 – 974, 2009. Mesoscopic Methods in Engineering and Science. 15, 17, 18

[13] Stphane Popinet. An accurate adaptive solver for surface-tension-driven interfacial flows. *Journal of Computational Physics"*, 228"(16"):5838 – 5866", 2009". 3

[14] S.A. Reijers. Lattice-Boltzmann simulation of laser-impact on a droplet. Master's thesis, Eindhoven University of Technology, 2015. 20

[15] Sebastian Schmieschek and Jens Harting. Contact angle determination in multicomponent lattice boltzmann simulations. *Communications in Computational Physics*, 9(5):11651178, 2011. 22

[16] Sudhir Srivastava. *Lattice Boltzmann Method for Contact Line Dynamics*. PhD thesis, Eindhoven University of Technology, 2014. 3, 14, 16, 17, 26, 27, 28, 29, 32

[17] Sauro Succi. Oxford. 14, 17, 27

[18] Sauro Succi. Lattice boltzmann 2038. *EPL (Europhysics Letters)*, 109(5):50001, 2015. 14, 17

[19] Michael C. Sukop and Daniel T. Thorne. *Lattice Boltzmann Modeling: An Introduction for Geoscientists and Engineers*. Springer Publishing Company, Incorporated, 1st edition, 2010. 13, 15, 16, 17, 21, 27

[20] Herman Wijshoff. The dynamics of the piezo inkjet printhead operation. *Physics Reports*, 491(4):77 – 177, 2010. 1

[21] Dieter A. Wolf-Gladrow. *Lattice-Gas, Cellular Automata and Lattice Boltzmann Models, An Introduction*, volume 1725 of *Lecture Notes in Mathematics*. Springer, Heidelberg, Berlin, 2000. 14

[22] Y. Yuan, T.R. Lee. *Surface Science Techniques*. Springer-Verlag Berlin Heidelberg, 2013. 12

Appendix A

Numerical results and parameters

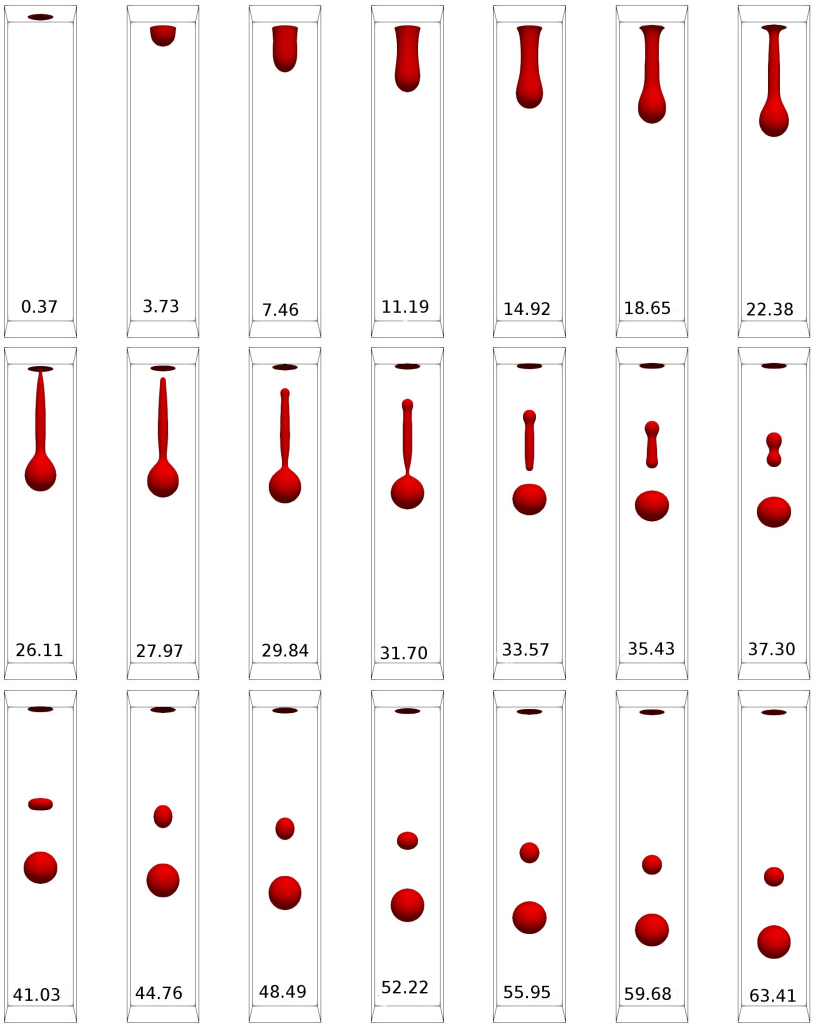

Figure A.1: Time series of qualitative numerical results of 3D liquid jetting, times are expressed in μs. The red color represents the liquid phase (isovolume of the density). Fig. 4.2 shows the geometry for this simulation and the parameters in SI and LU units are presented in table 4.3. In this simulation, the density ratio is $\rho_l/\rho_v = 214$.

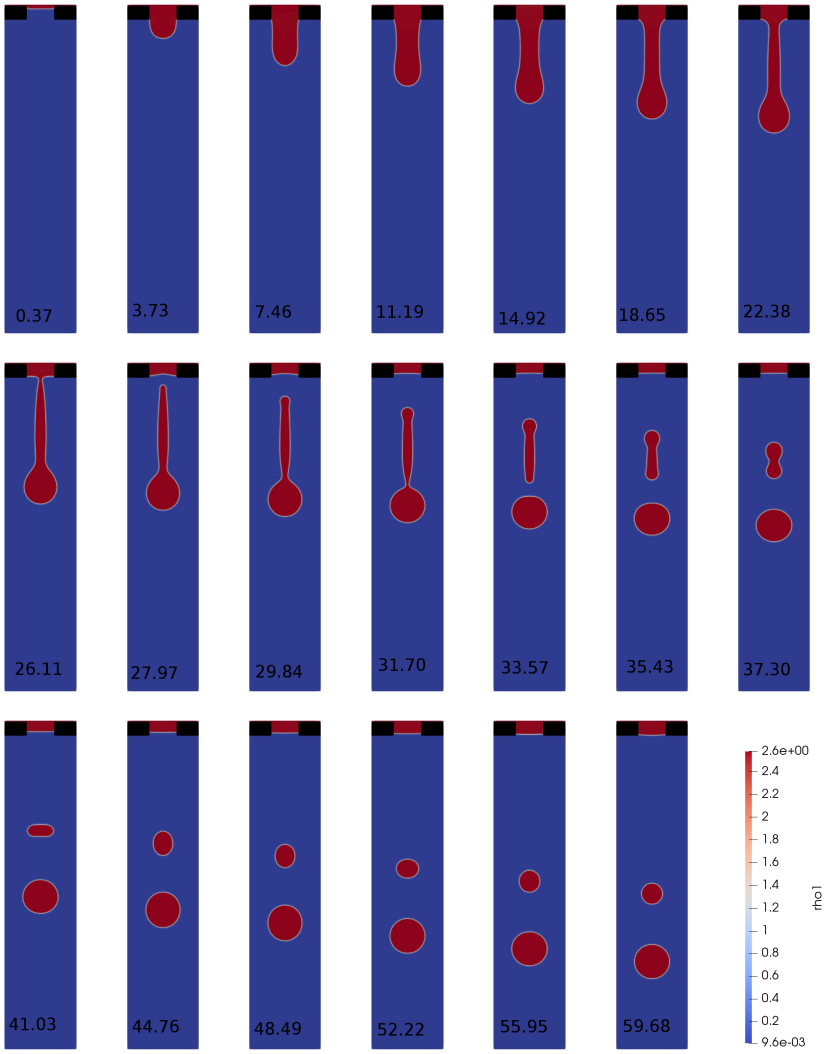

Figure A.2: Time series of a slice in the center of the domain showing the density field. The position of the head droplet, the tail droplet and the tip of the tail are plotted as a function of time in Fig. 4.8.

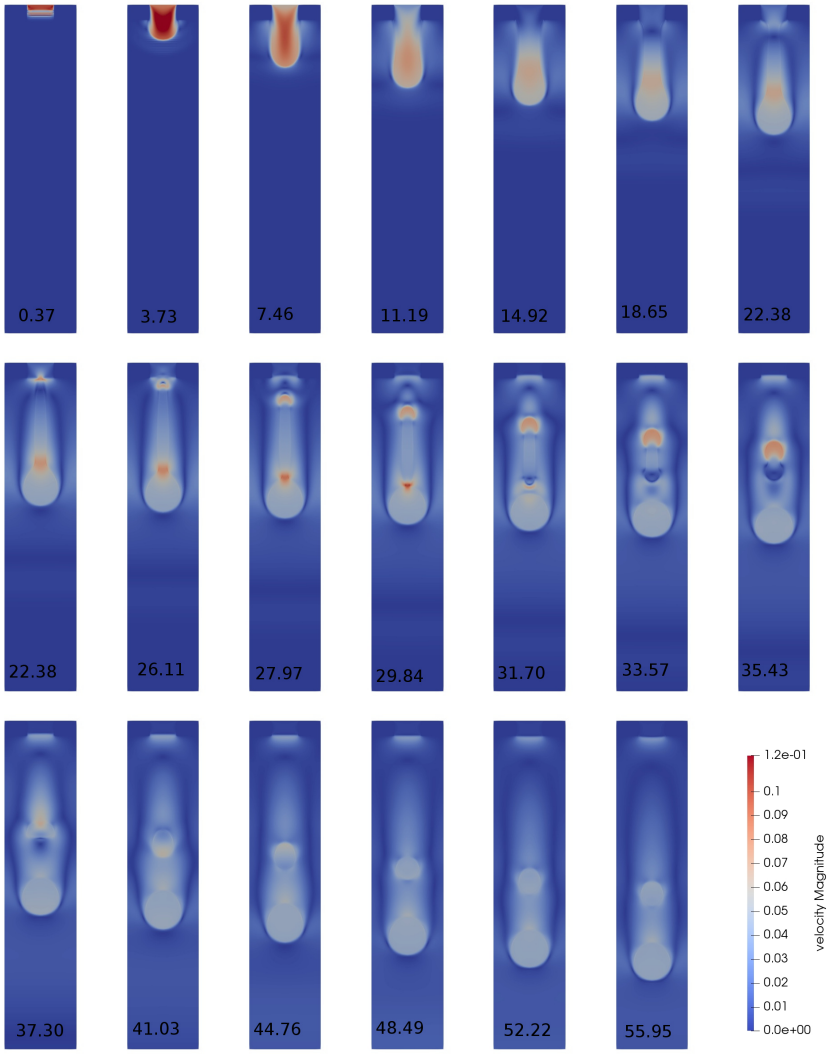

Figure A.3: Time series of a slice in the center of the domain showing the magnitude of the velocity field. The velocity of the head droplet, the tail droplet and the tip of the tail are plotted as a function of time in Fig. 4.8.